

# 中北大学硕士研究生指导教师资格 申请材料

姓 名： 王海宾

所在学院： 化学工程与技术学院


一级学科： 生物工程

2021 年 10 月

# 中北大学硕士研究生指导教师资格申请表

[illegible]

中北大学申请新增硕士研究生指导教师专家推荐表

申请人姓名		王海宾	职称	副教授	申请学科	生物工程
推荐人	姓名	胡志勇	职称	教授	所在学科	化学工程与技术
	研究方向	精细化学品的功能强化与应用开发				
<p>对申请人的推荐意见（包括思想品德、工作能力、专业基础、业务能力、科研经费及保障、外语水平等，请尽可能具体）</p> <p>王海宾同志热爱党、热爱社会主义，忠诚于党的事业，认真学习习近平新时代中国特色社会主义思想，积极投身于教育事业，秉承教书育人的理念，在日常的教学与管理工作中做出了突出贡献。</p> <p>王海宾同志多年来一直从事生物分离工程以及发酵工程的科研教学工作，具备坚实的理论基础、开阔的学术视野和求真务实的工作态度，不仅承担着山西省重点研发计划项目，而且积极与企业开展技术交流与合作，开展了沙棘综合利用、老陈醋生产过程中的发酵技术等研究，取得了较为显著的应用效果。他所承担的科研项目经费充足，为研究生培养提供了坚实的保障。</p> <p>该同志具备较高的英语运用水平，可以娴熟地查阅相关专业文献，且具有较好的英文写作能力。</p> <p>综上所述，王海宾同志具备了培养硕士研究生的能力且具备了开展科学研究所需的客观条件，特此推荐！</p> <div>推荐人签名： 2011年9月30日</div>						

中北大学申请新增硕士研究生指导教师专家推荐表

申请人姓名		王海宾	职称	副教授	申请学科	生物工程
推荐人	姓名	高莉	职称	副教授	所在学科	生物工程
	研究方向	生物药物与材料工程				
<p>对申请人的推荐意见（包括思想品德、工作能力、专业基础、业务能力、科研经费及保障、外语水平等，请尽可能具体）</p> <p>王海宾同志政治立场坚定，能够同党保持高度一致。该同志品德高尚，为人热情大方，乐于助人，善于团结身边的同志。</p> <p>该同志工作态度积极，善于发现问题和解决问题，具有较强的独立工作能力，担任生物工程专业本科生基础课《生物化学》授课任务，保持一丝不苟的工作作风，具有较强的敬业精神。该同志科研功底扎实，具有钻研精神，拥有较高的学术水平，主持 3 项省级课题，2 项横向课，参与多项国家级、省级课题，并且在科研工作中能够做到理论联系实际，可以在指导实践的实践中获得了横向课题科研合作经费。该同志英语水平较好，发表多篇高水平文章，协助指导硕士研究生 3 名。</p> <p>综上所述，王海宾同志综合素质高，科研工作能力强，相信能够胜任硕士研究生指导教师的工作，特此推荐申请硕士研究生导师。</p>						
<p>推荐人签名：高莉 2024 年 9 月 30 日</p>						



# 中北大学硕士研究生指导教师资格 申请支撑材料

- 1、学历、学位证明
- 2、任职资格证书
- 3、近三年的论文
- 4、近三年项目及经费到账证明

# 博士研究生 毕业证书



研究生王海宾 性别男，一九七五年十二月三十日生，于  
二〇〇八年九月至二〇一五年七月在 军事化学与烟火技术  
专业学习，学制三年，修完博士研究生培养计划规定的全部课程，成绩合格，  
毕业论文答辩通过，准予毕业。

培养单位：中北大学

校(院、所)长：

刘百智

证书编号：101101201501100010

二〇一五年七月一日

# 博士学位证书



王海宾，男，1975年12月30日生，在 中北大学

军事化学与烟火技术 学科(专业)已通过博士学位的课程

考试和论文答辩，成绩合格。根据《中华人民共和国学位条例》的规  
定，授予工学博士学位。

中北大学

校 长

学位评定委员会主席



证书编号：1011022015000002

二〇一五年六月二十四日



姓名 王海宾  
性别 男  
出生年月 1975年12月  
工作单位 中北大学  
序号: N0 201205975

16  
评审委员会 中北大学教师高级职称评审委员会  
名称

评审通过 副教授  
任职资格

专业 生物化工

评审通过 2012年09月05日  
时间

发证单位 山西省人力资源和社会保障厅 (章)

发证日期 2013年4月28日

编号: 010029167

## 国家级大学生创新创业训练计划平台

National Students' platform for innovation and entrepreneurship training program

2019  
23  
期星

首页 历年项目 通知公告 咨询问答 下载专区 欢迎您! 您是第 0000000000435536 人

您现在的位置: 首页 >> 立项项目 >> 生物学 >> 沙棘黄酮快速检测方法的研究与开发

项目编号: 201810110007

项目名称: 沙棘黄酮快速检测方法的研究与开发

项目关键词:

项目类型: 创新训练项目

所属学校: 中北大学

项目实施时间: 至

所属一级学科: 生物学

所属二级学科:

立项时间: 2018-05-31

批准经费额度: 14000.00(元)

项目成员:

姓名	年级	学号	所在院系	专业	联系电话	E-mail	是否主持人
李静		1604064105					第一主持人
吕楠		1604064106					否
赵丰田		1604064250					否
黄庆恩		1604064247					否
郭仕伟		1604064226					否


指导教师:

[第一指导教师]姓名: 王海宾, 单位: , 专业技术职务: 副教授





## 文献收录/引用检索证明

委托人	王海滨	委托人单位	中北大学
委托内容	<p>检索以下题名的文献被 SCI-E 数据库 (Science Citation Index Expanded) 收录情况:</p> <ol style="list-style-type: none"> <li>1、Ni-Co LDH/M-Mo-S (M = Zn, Co and Ni) nanoarrays as efficient water oxidation electrocatalytic materials</li> <li>2、Synthesis of two 3D supramoleculars and their fluorescent sensing for nitroaromatic compounds/Fe<sup>3+</sup> ions in aqueous medium</li> </ol>		
检索数据库	Science Citation Index Expanded		
检索结果	<p>委托检索的文献均被 SCI-E 数据库收录。</p> <p>检索结果见检索页。</p> <p>特此证明!</p>		
检索机构	<div style="text-align: center;">  <p>中北大学图书馆查新中心</p> <p>查新专用章</p> </div>		
检索日期	2021 年 9 月 30 日	检索人	田艳玲 (签字)

## 第 1 条, 共 2 条

标题: Ni-Co LDH/M-Mo-S (M = Zn, Co and Ni) nanoarrays as efficient water oxidation electrocatalytic materials

作者: Wang, HB (Wang, Haibin); Zhang, XS (Zhang, Xiaoshuang)

来源出版物: CRYSTENGCOMM 卷: 23 期: 15 页: 2862-2868 DOI: 10.1039/d1ce00247c 提前访问日期: MAR 2021 出版年: APR 21 2021

Web of Science 核心合集中的 "被引频次": 0

被引频次合计: 0

入藏号: WOS:000635215100001

地址: [Wang, Haibin] North Univ China, Sch Chem Engn &amp; Technol, Taiyuan 030051, Peoples R China.

[Zhang, Xiaoshuang] North Univ China, Sch Sci, Taiyuan, Peoples R China.

通讯作者地址: Zhang, XS (通讯作者), North Univ China, Sch Sci, Taiyuan, Peoples R China.

电子邮件地址: 20160068@nuc.edu.cn

IDS 号: RP7KP

eISSN: 1466-8033



## 第 2 条, 共 2 条

标题: Synthesis of two 3D supramoleculars and their fluorescent sensing for nitroaromatic compounds/Fe<sup>3+</sup> ions in aqueous medium

作者: Wang, HB (Wang, Haibin); Gao, T (Gao, Ting); Zhang, YJ (Zhang, Yujuan)

来源出版物: INORGANIC CHEMISTRY COMMUNICATIONS 卷: 122 文献号: 108293 DOI: 10.1016/j.inoche.2020.108293 出版年: DEC 2020

Web of Science 核心合集中的 "被引频次": 0

被引频次合计: 0

入藏号: WOS:000600416900005

地址: [Wang, Haibin; Gao, Ting; Zhang, Yujuan] North Univ China, Sch Chem Engn &amp; Technol, Taiyuan 030051, Peoples R China.

通讯作者地址: Zhang, YJ (通讯作者), North Univ China, Sch Chem Engn &amp; Technol, Taiyuan 030051, Peoples R China.

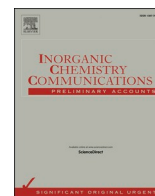
电子邮件地址: 491813789@qq.com

IDS 号: PH4XG

ISSN: 1387-7003

eISSN: 1879-0259





## Short communication

Synthesis of two 3D supramoleculars and their fluorescent sensing for nitroaromatic compounds/ $\text{Fe}^{3+}$  ions in aqueous mediumHaibin Wang, Ting Gao, Yujuan Zhang<sup>\*</sup>

School of Chemical Engineering and Technology, North University of China, Taiyuan 030051, PR China

## ARTICLE INFO

## Keywords:

Supramolecular  
Fluorescent sensing  
Nitroaromatic compounds  
 $\text{Fe}^{3+}$  ions  
Aqueous solution

## ABSTRACT

Two 2D coordination polymers (CPs), namely,  $\{[\text{Cu}(\text{bib})_2] \cdot 2\text{NO}_3 \cdot \text{H}_2\text{O}\}_n$  (**1**) and  $\{[\text{Zn}_3(\text{bib})_{2.5}(\text{C}_2\text{O}_4)_3(\text{H}_2\text{O})] \cdot \text{DMF} \cdot \text{H}_2\text{O}\}_n$  (**2**) {bib = 1,4-bis (1-imidazoly) benzene} have been synthesized under solvothermal conditions. The structural analysis revealed that both **1** and **2** are 2D frameworks, which are further expanded into 3D supramolecular structures through C—H...O hydrogen bonding. Luminescence properties reveal that **1/2** has highly sensitive and selective recognition for nitroaromatic compounds (NACs)/ $\text{Fe}^{3+}$  ions in aqueous solutions. Moreover, the luminescence quenching mechanisms were systematically revealed via photoinduced electron transfer (PET) process, resonance energy transfer (RET) and fluorescence lifetime.

## 1. Introduction

With the development of industry, more and more types of pollutants threaten human safety and health. Nitroaromatic compounds (NACs) are not only intermediates of fine chemicals such as medicines, dyes, and leather, but also the main components of explosives, making a great contribution to the progress of the industry [1–5]. However, in the past few years, a large number of NACs from factories and laboratories have been discharged into lakes and rivers, and have caused great harm to the environment [6]. Iron is one of the essential elements of the human body [7–10]. Due to the massive discharge of industrial wastewater, the content of iron in the ecosystem has increased. But excessive iron in the human body can cause liver cirrhosis, osteoporosis and diabetes [11,12]. Therefore, it is urgent to find a suitable material that can sensitively and selectively detect target pollutants in the environment [13].

At present, the methods for detecting the above-mentioned pollutants mainly include ion chromatography, ion mobility spectrometry, surface-enhanced Raman spectroscopy and inductively coupled plasma, but these methods have some disadvantages of complicated operations and expensive cost [14–20]. In recent years, coordination polymers (CPs) with excellent optical properties and controllable structures have caused extensive attention by chemists due to their potential application in identifying pollutants [21–31]. Tsai *et al.* have reported a series of Zn (II) CPs as efficient fluorescent sensors for detecting NACs in toluene [32]. Zhang *et al.* have synthesized luminescent CPs for sensing 2,4,6-trinitrophenol in DMF solution [33]. So far, the detection of the above-

mentioned pollutants, especially NACs, was mainly carried out in organic solvents. This makes the identification of pollutants unfavorable for practical applications, and at the same time causes secondary pollution to the environment [34].

Based on the above situation, 1,4-bis (1-imidazoly) benzene (bib) was selected to construct the title CPs based on the following considerations: (a) The structure of CPs is easy to control due to its simple coordination mode. (b) It can be used as a hydrogen bond acceptor to facilitate the construction of a 3D supramolecular structure [35]. Herein, two 3D supramolecular CPs, namely,  $\{[\text{Cu}(\text{bib})_2] \cdot 2\text{NO}_3 \cdot \text{H}_2\text{O}\}_n$  (**1**) and  $\{[\text{Zn}_3(\text{bib})_{2.5}(\text{C}_2\text{O}_4)_3(\text{H}_2\text{O})] \cdot \text{DMF} \cdot \text{H}_2\text{O}\}_n$  (**2**), have been successfully prepared (Scheme S1 and Scheme S2). In addition, luminescence sensing experiments of **1** and **2** were investigated in aqueous solution in detail. Meanwhile, the luminescence quenching mechanisms of NACs and  $\text{Fe}^{3+}$  ions for **1** and **2** were also explored by photoinduced electron transfer (PET) process, resonance energy transfer (RET) and fluorescence lifetime.

## 2. Synthesis of compounds

2.1. Synthesis of  $\{[\text{Cu}(\text{bib})_2] \cdot 2\text{NO}_3 \cdot \text{H}_2\text{O}\}_n$  (**1**)

A mixture of  $\text{Cu}(\text{NO}_3)_2 \cdot 3\text{H}_2\text{O}$  (0.012 mmol, 2.5 mg), bib (0.004 mmol, 0.8 mg), DMF/ $\text{H}_2\text{O}$  (1 mL, v/v = 1/4) and NaOH solution (0.2 mol/L, 0.05 mL) was added to the hard glass tube, pumped into a near-vacuum, heated to 85 °C for 3000 mins and cooled naturally to 25 °C.

<sup>\*</sup> Corresponding author.E-mail address: [491813789@qq.com](mailto:491813789@qq.com) (Y. Zhang).<https://doi.org/10.1016/j.inoche.2020.108293>

Received 7 September 2020; Received in revised form 5 October 2020; Accepted 5 October 2020

Available online 15 October 2020

1387-7003/© 2020 Elsevier B.V. All rights reserved.

Purple block crystals of **1** were obtained by washing three times alternately with mother liquor. Yield: 43% based on bib. Anal. (%) calcd. for  $C_{24}H_{22}N_{10}O_7Cu$ : C, 47.48; H, 3.63; N, 23.08. Found (%): C, 48.01; H, 6.49; N, 22.97. IR (KBr pellet,  $cm^{-1}$ ): 3113 (m), 2373 (vs), 1938 (w), 1830 (w), 1554 (s), 1507 (m), 1394 (m), 1278 (w), 1132 (s), 1067 (s), 982 (m), 832 (m), 664 (s), 537 (w) (Fig. S1a).

## 2.2. Synthesis of $\{[Zn_3(bib)_{2.5}(C_2O_4)_3(H_2O)] \cdot DMF \cdot H_2O\}_n$ (**2**)

$Zn(NO_3)_2 \cdot 6H_2O$  (0.012 mmol, 3.6 mg), bib (0.004 mmol, 0.8 mg) and  $C_2H_4O_4 \cdot 2H_2O$  (0.008 mmol, 1.0 mg) were dissolved in 1 mL DMF/ $H_2O$  (v/v = 1/1) mixed solution, which was sealed to the hard glass tube under vacuum, heated to 120 °C for 3000 mins and slowly cooled to ambient temperature. Colorless block crystals of **2** were gained by filtering and washing with mother liquor. Yield: 47% based on bib. Anal. (%) calcd. for  $C_{75}H_{65}N_{21}O_{29}Zn_6$ : C, 42.52; H, 3.07; N, 13.89. Found (%): C, 42.46; H, 3.12; N, 13.71. IR (KBr pellet,  $cm^{-1}$ ): 3398 (m), 3138 (w), 2362 (m), 1702 (m), 1610 (s), 1528 (m), 1307 (vs), 1143 (m), 1061 (vs), 960 (m), 839 (m), 801 (s), 733 (m), 642 (m), 542 (w) (Fig. S1b).

## 3. Results and discussion

### 3.1. Structural descriptions

#### 3.1.1. $\{[Cu(bib)_2] \cdot 2NO_3 \cdot H_2O\}_n$ (**1**)

The structural analysis indicates that **1** crystallizes in the orthorhombic crystal system  $Pcan$  space group. The asymmetric unit contains one independent Cu (II) ion, two bib ligands, two lattice  $NO_3$  ions and one lattice  $H_2O$  molecule (Fig. 1). Each Cu (II) ion is tetra-coordinated by four N-atoms from four different bib ligands ( $Cu(1) - N(2) = 1.9845$  (95) Å,  $Cu(1) - N(2)B = 1.9845$  (49) Å,  $Cu(1) - N(5)A = 2.0073$  (48) Å,  $Cu(1) - N(5)C = 2.0073$  (48) Å), displaying a quadrangular geometry. The bond angles around the Cu (II) ion are 89.608 (193)° and 90.392 (193)° (Table S2), which are consistent with the reported Cu-CPs [36].

As can be seen from Fig. S2, the bib ligands with *trans*-conformation connect with Cu (II) ions by a bridging pattern to construct 1D  $[Cu(bib)]_n$  chains with the distance between  $Cu \cdots Cu$  being 13.0803 (17) Å, which are bridged by bib ligands to form 2D layered structures. Moreover, as shown in Fig. 2, the 2D layer is further extended into a 3D supramolecular structure via  $C-H \cdots O$  hydrogen bonds between bib ligands and lattice  $NO_3$  ions (Table S3).

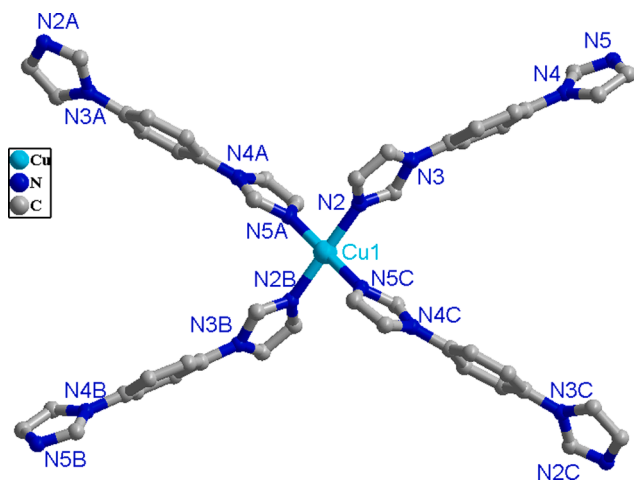


Fig. 1. Coordination environment of the Cu (II) in **1**. Hydrogen atoms are omitted for clarity. (Symmetry codes: A:  $1.5 - x, 0.5 - y, 0.5 + z$ ; B:  $1 - x, 1 - y, 1 - z$ ; C:  $-0.5 + x, 0.5 + y, 0.5 - z$ ).

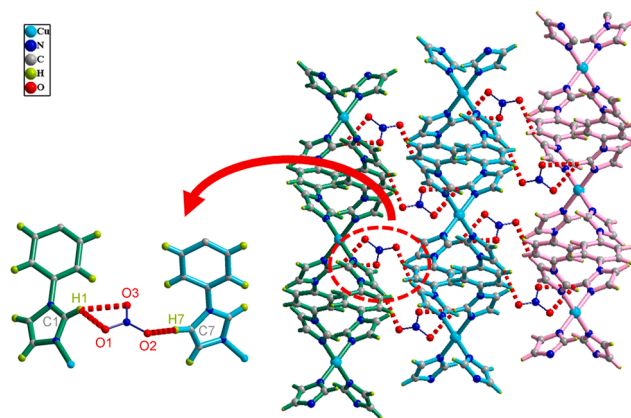


Fig. 2. A 3D supramolecular structure of **1** formed by hydrogen bonds interactions.

#### 3.1.2. $\{[Zn_3(bib)_{2.5}(C_2O_4)_3(H_2O)] \cdot DMF \cdot H_2O\}_n$ (**2**)

The structural analysis reveals that **2** crystallizes in the triclinic system  $P-1$  space group. As depicted in Fig. 3, the asymmetric unit of **2** consists of three Zn (II) ions, two and a half bib ligands, three oxalate molecules, one coordinated  $H_2O$  molecule, one lattice DMF molecule and one lattice  $H_2O$  molecule. Both Zn1 (II) and Zn2 (II) ions are six-coordinated by two N-atoms of two different bib ligands and four O-atoms of two oxalate, exhibiting irregular octahedral geometries. Although the Zn3 (II) ion is also six coordinated and presents a distorted octahedral geometry, it is surrounded by one N-atom from bib linker and five O-atoms from two oxalate and one coordinated  $H_2O$  molecule (Fig. S3d). The Zn-O/N bond distances are between 2.054 (3) Å and 2.183 (3) Å. The bond angles around Zn (II) ions vary from 77.75 (9) to 172.81 (10)° (Table S2), which are in accordance with the values reported in the literature [37].

In Fig. S3, oxalate adopts a chelated coordination mode to link with Zn (II) ions forming a trinuclear cluster with the nearest  $Zn \cdots Zn$  distance of 5.4065 (8) Å, which is expanded by oxalate to form 1D left-handed and right-handed helix chains, which are further linked by bib ligands to form 2D layered structures. Finally, the 2D layer is expanded into a 3D supramolecular structure (Fig. 4) through  $C-H \cdots O$  hydrogen bonds between oxalate and bib ligands (Table S4).

### 3.2. Powder X-ray diffraction (PXRD) analysis and thermal analysis

PXRD patterns of **1** and **2** were measured to verify their phase purity. As exhibited in Fig. S4 that the experimental diffraction patterns of **1** and **2** are basically consistent with those of the simulated ones. To further investigate the chemical stability of CPs **1** and **2**, the PXRD patterns of **1** and **2** soaked in water for 4 h, 8 h, 12 h and 24 h were recorded. As shown in Fig. S5, the PXRD patterns of the samples immersed in aqueous solution for different times are basically the same as those of the as-

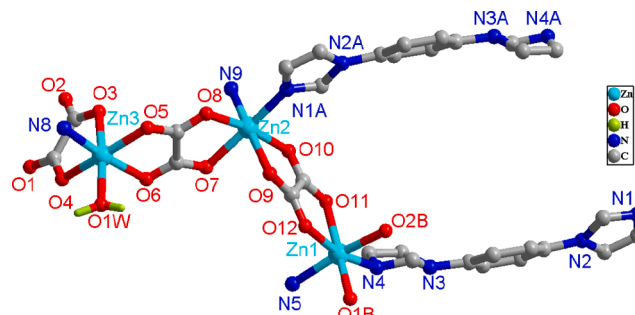


Fig. 3. Coordination environment of the metal Zn (II) in **2**. (Symmetry codes: A:  $-1 - x, 1 - y, 1 - z$ ; B:  $-1 + x, -1 + y, z$ ).



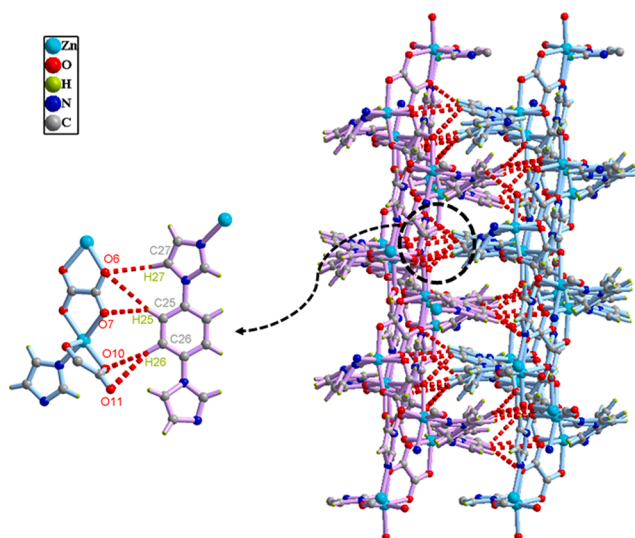


Fig. 4. A 3D supramolecular structure of **2** obtained by H-bonding interactions.

prepared ones, indicating that CPs **1** and **2** have higher water stability, which can be attributed to the intramolecular hydrogen bonding [38]. The thermal stability of **1** and **2** at 25–800 °C was measured under N<sub>2</sub> atmosphere (Fig. S6). As for **1**, the weight loss of 2.83% (calcd. 2.87%) was attributed to the release of one lattice water molecule between 75 °C and 103 °C, and the weight loss of 19.82% (calcd. 19.80%) was ascribed to the release of two lattice NO<sub>3</sub><sup>−</sup> in the temperature range of 103–170 °C. Then, the framework of **1** began to collapse above 435 °C. For **2**, the obvious weight loss of 1.88% (calcd. 1.64%) was attributed to the removal of one lattice water in the temperature range of 80–120 °C, the weight loss of 8.26% corresponds to the release of one coordinated water molecule and one free DMF molecule (calcd. 8.32%) at 240–300 °C. The framework of **2** began to collapse above 390 °C.

### 3.3. Luminescent sensing

As shown in Fig. 5, the solid state fluorescence spectra of bib ligand, **1** and **2** were measured at room temperature. The main emission peak of free bib ligand is observed at 343 nm ( $\lambda_{\text{ex}} = 275$  nm), which may be attributed to the  $n \rightarrow \pi^*$  or  $\pi \rightarrow \pi^*$  transitions [39,40]. Meanwhile, **1** and **2** exhibit the emission peaks at 343 nm and 360 nm ( $\lambda_{\text{ex}} = 275$  nm), respectively. Compared with the free bib ligand, the emission peak of **2** is slightly red-shifted, which can be assigned to the effect of coordination

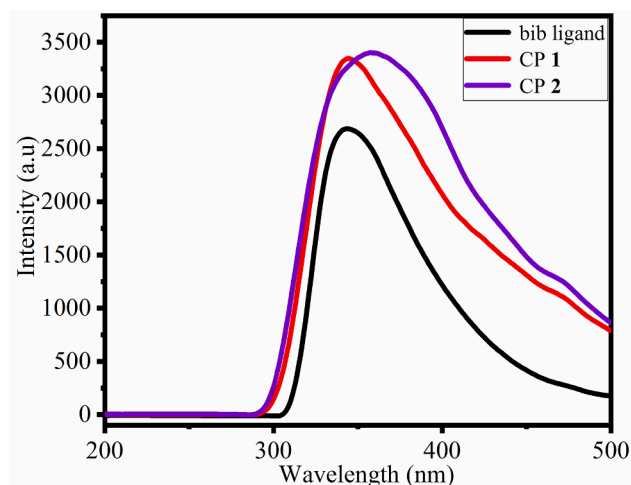


Fig. 5. The emission spectra of **1**, **2** and bib ligand.

[41,42].

#### 3.3.1. Sensing of NACs

In view of the excellent fluorescence properties of **1** and **2**, the fluorescent sensing performances of **1** and **2** for NACs, including nitrobenzene (NB), nitrotoluene (NT), nitrophenol (NP), nitroaniline (NA), were explored in aqueous solution. 2.0 mg finely ground samples were dispersed in 2 mL aqueous solution of NACs with different concentrations, respectively, and treated with the ultrasonic waves for 30 mins to form uniform suspensions.

As shown in Fig. 6, the luminescence intensities of **1** and **2** gradually decreased with the rise of NACs concentration. Among NACs, NP has the most obvious quenching effect on CPs and the quenching order of NACs for CPs follows NP > NB > NT > NA. In addition, the Stern–Volmer equation was used to explain the relationship between  $I_0/I$  and the concentration of NACs. As summarized in Fig. S7 and S8, the plot of  $I_0/I$  vs the concentration of NACs is linear at lower concentration, where  $I_0$  and  $I$  are the luminescence intensities without and with NACs, respectively. Meanwhile, the  $K_{\text{sv}}$  values of title CPs for NACs were calculated to be  $1.5 \times 10^4 \text{ M}^{-1}$  (NP),  $9.8 \times 10^3 \text{ M}^{-1}$  (NB),  $4.4 \times 10^3 \text{ M}^{-1}$  (NT),  $2.3 \times 10^3 \text{ M}^{-1}$  (NA) for **1** and  $9.8 \times 10^3 \text{ M}^{-1}$  (NP),  $6.5 \times 10^3 \text{ M}^{-1}$  (NB),  $6.4 \times 10^3 \text{ M}^{-1}$  (NT),  $2.5 \times 10^3 \text{ M}^{-1}$  (NA) for **2**. In addition, the detection limits for NACs obtained by the formula of  $3\delta/k$  ( $\delta$  is the standard deviation of the fluorescence intensity data), were  $7.6 \times 10^{-5} \text{ M}$  (NP),  $1.1 \times 10^{-4} \text{ M}$  (NB),  $2.5 \times 10^{-4} \text{ M}$  (NT),  $4.9 \times 10^{-4} \text{ M}$  (NA) for **1** and  $1.1 \times 10^{-4} \text{ M}$  (NP),  $1.7 \times 10^{-4} \text{ M}$  (NB),  $1.7 \times 10^{-4} \text{ M}$  (NT),  $4.5 \times 10^{-4} \text{ M}$  (NA) for **2** (Table S5). When the concentration of NACs reaches 1 mM, the quenching efficiencies of CPs are 99.32% (NP), 97.67% (NB), 87.73% (NT) and 80.36% (NA) for **1**, and 98.91% (NP), 94.45% (NB), 89.99% (NT) and 80.06% (NA) for **2**, respectively (Fig. S9 and Fig. S10).

The luminescent quenching mechanisms of NACs for **1/2** were explored. Firstly, the PXRD patterns of **1/2** after the fluorescence experiments are basically consistent with those of the simulated ones with single crystal data (Fig. S11), which rules out that fluorescence quenching was caused by the structural collapse. Secondly, as depicted in Fig. 7, the lowest unoccupied molecular orbitals (LUMO) energy of the bib ligand obtained by using the density functional theory (DFT) at the B3LYP/6-31G\* level is higher than the LUMO energy of the NACs, which makes the electrons transfer from the bib ligand of **1/2** to the LUMOs of NACs, resulting in fluorescence quenching. The lower the

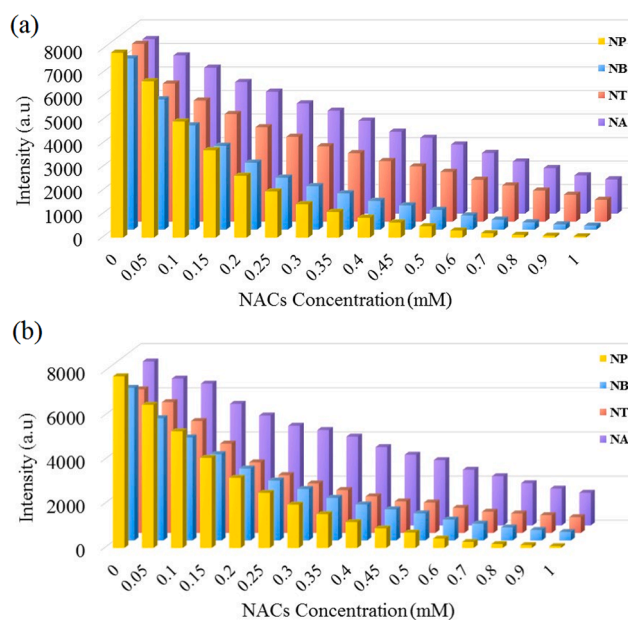


Fig. 6. The luminescence intensities of **1** (a) and **2** (b) when the NACs concentration is in the ranges of 0–1 mM.

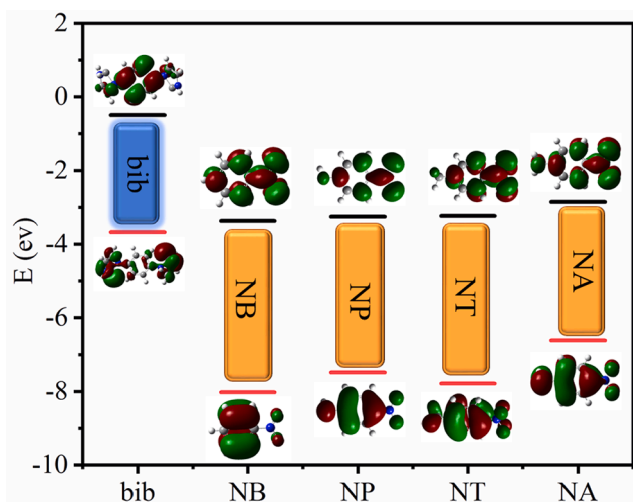


Fig. 7. HOMO and LUMO energies for the selected NACs, free bib ligand.

LUMO energy of NACs, the better the quenching effect [43,44]. However, the quenching order of  $\text{NP} > \text{NB} > \text{NT} > \text{NA}$  is not consistent with the quenching order of  $\text{NB} > \text{NP} > \text{NT} > \text{NA}$  based on LUMO energy, which indicates that the PET process is not the only cause of fluorescence quenching. Thirdly, as shown in Fig. S12, there is an obvious overlap between the emission spectra of 1/2 and the absorption spectra of NACs. The spectral overlap degree ( $\text{NP} > \text{NB} > \text{NT} > \text{NA}$ ) of NACs and 1/2 is exactly consistent with the luminescent quenching of NACs for 1/2. This result clearly demonstrated that RET processes occurred between NACs and 1/2 [45]. Finally, the fluorescence lifetime of the 1/2 before and after fluorescence sensing NACs experiments were tested (Fig. S13 and Fig. S14). As summarized in Table S8 that the fluorescence lifetime of 1/2 is basically unchanged after sensing NACs, which reveals that fluorescence quenching is static process.

### 3.3.2. Sensing of cations

The ground powder samples of 1 and 2 (2 mg) are dispersed in 2 mL  $\text{M}(\text{NO}_3)_n$  aqueous solutions (0.01 mol/L,  $\text{M} = \text{Na}^+, \text{Ag}^+, \text{K}^+, \text{Ca}^{2+}, \text{Cu}^{2+}, \text{Co}^{2+}, \text{Ni}^{2+}, \text{Mn}^{2+}, \text{Ba}^{2+}, \text{Zn}^{2+}, \text{Cd}^{2+}, \text{Pb}^{2+}, \text{Hg}^{2+}, \text{Fe}^{2+}, \text{Al}^{3+}$  and  $\text{Fe}^{3+}$ )

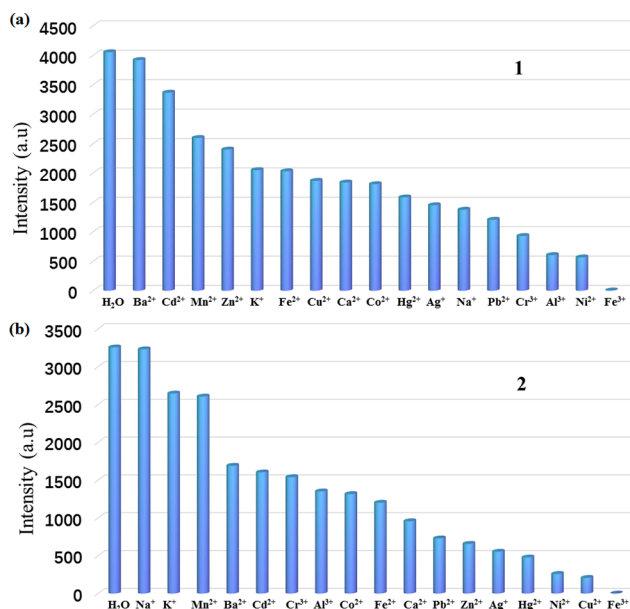


Fig. 8. The luminescence intensities of 1 (a) and 2 (b) in aqueous solutions containing different metal ions.

by ultrasonic treatment for 30 mins to form uniform suspensions.

As shown in Fig. 8, when  $\text{Fe}^{3+}$  was added to 1 and 2, the fluorescence intensities of 1 and 2 were significantly quenched compared with other ions. The quenching effect of  $\text{Fe}^{3+}$  for 1 and 2 was further explored. As shown in Fig. 9, the fluorescence intensities of 1 and 2 gradually decreased with the addition of  $\text{Fe}^{3+}$ . When  $\text{Fe}^{3+}$  ions (1 mM) were added, and the quenching efficiency reached 99% (Fig. S15). Meanwhile, the quenching efficiency can be quantitatively evaluated by  $K_{\text{SV}}$  based on the Stern–Volmer equation:  $I_0/I = 1 + K_{\text{SV}}[Q]$ , where  $I_0$  and  $I$  are the luminescence intensities without and with  $\text{Fe}^{3+}$  ions, respectively,  $K_{\text{SV}}$  is the quenching constant and  $[Q]$  is the concentration of  $\text{Fe}^{3+}$  ions. As shown in Fig. S16, there was a good linear relationship between  $I_0/I$  and the concentration of  $\text{Fe}^{3+}$  ions at lower concentration, and  $K_{\text{SV}}$  was calculated to be  $1.2 \times 10^5 \text{ M}^{-1}$  for 1 and  $8.9 \times 10^4 \text{ M}^{-1}$  for 2, which were higher than those of recently reported CPs luminescent sensors for the detection of  $\text{Fe}^{3+}$  ions [46–49] (Table S6). Moreover, the detection limits for  $\text{Fe}^{3+}$  ions were  $2.78 \times 10^{-6} \text{ M}$  for 1 and  $4.99 \times 10^{-6} \text{ M}$  for 2 (Table S7). Furthermore, the anti-interference experiments of 1/2 toward  $\text{Fe}^{3+}$  ions in the presence of other ions were carried out. As shown in Fig. S17, when  $\text{Fe}^{3+}$  ions were added to the aqueous solution containing other metal ions, the luminescence intensities decline sharply, indicating that 1/2 shows good selectivity for  $\text{Fe}^{3+}$  ions.

The luminescent quenching mechanisms of  $\text{Fe}^{3+}$  for 1/2 were researched. As illustrated in Fig. S18, the PXRD patterns of 1/2 after fluorescence tests are well-matched with those simulated from the single crystal data of 1/2, which reveals that the luminescence quenching of 1/2 is not caused by the collapse of the structure. Meanwhile, compared with other metal ions, the UV absorption spectra of  $\text{Fe}^{3+}$  ion and the emission spectra of 1/2 have greater overlap (Fig. S19), so the fluorescence quenching caused by  $\text{Fe}^{3+}$  ions can be attributed to the RET mechanism [50]. In addition, the fluorescence lifetime of 1/2 after sensing  $\text{Fe}^{3+}$  ion is basically the same as that of the as-prepared 1/2 (Fig. S13, Fig. S14 and Table S8), which indicates that fluorescence quenching is static process [51].

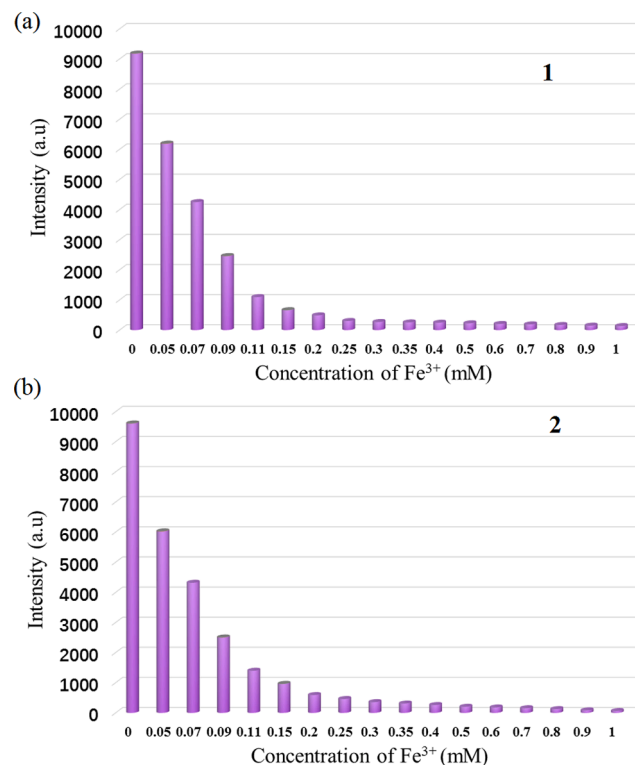


Fig. 9. The luminescence intensities of 1 (a) and 2 (b) when the  $\text{Fe}^{3+}$  concentration is the ranges of 0–1 mM.

## 4. Conclusion

Two 3D supramoleculars were solvothermally synthesized. Meanwhile, fluorescence experiments revealed that **1/2** has highly selective and sensitive sensing toward NACs/ $\text{Fe}^{3+}$  ions in aqueous solutions with low detection limits. The quenching mechanisms of the analytes for **1/2** are attributed to PET, RET and static process for NACs, and RET and static process for  $\text{Fe}^{3+}$ , respectively. These results indicate that the title CPs can be used as potential fluorescent sensors for the detection of NACs/ $\text{Fe}^{3+}$  ions in aqueous medium.

## CCRediT authorship contribution statement

**Haibin Wang:** Writing - original draft. **Ting Gao:** Data curation. **Yujuan Zhang:** Data curation, Writing - review & editing.

## Declaration of Competing Interest

The authors declare that they have no known competing financial interests or personal relationships that could have appeared to influence the work reported in this paper.

## Acknowledgements

The authors gratefully acknowledge the financial support of this work by the Natural Science Foundation of China (Grant 21676258), Central Leading Local Science and Technology Development Special Fund Project (YDZX20191400002636), the international Scientific and Technological Cooperation Projects of Shanxi Province (201803D421080), Science and Technology Innovation Project of Shanxi Province Colleges and Universities (2020CG037) and Shanxi Province Graduate Education Innovation Project (2020SY383).

## Appendix A. Supplementary material

CCDC 2024775 and 2024776 contains the supplementary crystallographic data for **1** and **2**. These data can be obtained free of charge via <http://www.ccdc.cam.ac.uk/conts/retrieving.html>, or from the Cambridge Crystallographic Data Centre, 12 Union Road, Cambridge CB2 1EZ, UK; fax: (+44) 1223-336-033; or e-mail: [deposit@ccdc.cam.ac.uk](mailto:deposit@ccdc.cam.ac.uk).

Supplementary data to this article can be found online at <https://doi.org/10.1016/j.inoche.2020.108293>.

## References

- X. Wang, Y. Han, X.X. Han, X. Hou, J.-J. Wang, F. Fu, Highly selective and sensitive detection of  $\text{Hg}^{2+}$ ,  $\text{Cr}_2\text{O}_7^{2-}$ , and nitrobenzene/2,4-dinitrophenol in water via two fluorescent Cd-CPs, *New J. Chem.* 42 (2018) 19844–19852.
- W. Liu, X. Huang, C. Xu, C. Chen, L. Yang, W. Dou, W. Chen, H. Yang, W. Liu, A Multi-responsive regenerable europium-organic framework luminescent sensor for  $\text{Fe}^{3+}$ ,  $\text{Cr}^{\text{VI}}$  anions, and picric acid, *Chem. Eur. J.* 22 (2016) 18769–18776.
- H. Xu, F. Liu, Y. Cui, B. Chen, G. Qian, A luminescent nanoscale metal-organic framework for sensing of nitroaromatic explosives, *Chem. Commun.* 47 (2011) 3153–3155.
- J.X. Liang, J. Zhang, J.F. Liang, L.J. Zhai, H.N. Wu, X.Y. Niu, T.P. Hu, Five new coordination polymers with a Y-shaped N-heterocyclic carboxylic acid: structural diversity, bifunctional luminescence sensing and magnetic properties, *CrystEngComm* 21 (2019) 5767–5778.
- J. Shen, J. Zhang, Y. Zuo, L. Wang, X. Sun, J. Li, W. Han, R. He, Biodegradation of 2,4,6-trinitrophenol by rhodococcus sp. isolated from a picric acid-contaminated soil, *J. Hazard. Mater.* 163 (2009) 1199–1206.
- Y. Salinas, R. Martinez-Manez, M.D. Marcos, F. Sancenon, A.M. Costero, M. Parra, S. Gil, Optical chemosensors and reagents to detect explosives, *Chem. Soc. Rev.* 41 (2012) 1261–1296.
- S. Sanda, S. Parshamoni, S. Biswas, S. Konar, Highly selective detection of palladium and picric acid by a luminescent MOF: a dual functional fluorescent sensor, *Chem. Commun.* 51 (2015) 6576–6579.
- F.L. Hu, Y.X. Shi, H.H. Chen, J.P. Lang, A Zn(II) coordination polymer and its photocycloaddition product: syntheses, structures, selective luminescence sensing of iron(III) ions and selective absorption of dyes, *Dalton Trans.* 44 (2015) 18795–18803.
- Z.J. Li, X.Y. Li, Y.T. Yan, L. Hou, W.Y. Zhang, Y.Y. Wang, Tunable emission and selective luminescence sensing in a series of lanthanide metal-organic frameworks with uncoordinated Lewis basic triazolyl sites, *Cryst. Growth Des.* 18 (2018) 2031–2039.
- S. Chen, Z. Shi, L. Qin, H. Jia, H. Zheng, Two new luminescent Cd (II)-metal-organic frameworks as bifunctional chemosensors for detection of cations  $\text{Fe}^{3+}$ , anions  $\text{CrO}_4^{2-}$ , and  $\text{Cr}_2\text{O}_7^{2-}$  in aqueous solution, *Cryst. Growth Des.* 17 (2017) 67–72.
- Y. Di, X. Cui, Y. Liu, C. Zhou, Y. Di, One novel functional Cd-CPs as luminescent sensor for efficient sensing of  $\text{Fe}^{3+}$  cations in aqueous solution, *Inorg. Chem. Commun.* 108 (2019) 107491–107495.
- Z. Chen, Y. Sun, L. Zhang, D. Sun, F. Liu, Q. Meng, R. Wang, D. Sun, A tubular europium-organic framework exhibiting selective sensing of  $\text{Fe}^{3+}$  and  $\text{Al}^{3+}$  over mixed metal ions, *Chem. Commun.* 49 (2013) 11557–11559.
- B. Dutta, A. Hazra, A. Dey, C. Sinha, P.P. Ray, P. Banerjee, M.H. Mir, Construction of a succinate bridged Cd(II)-based 2D coordination polymer for efficient optoelectronic device fabrication and explosive sensing application, *Cryst. Growth Des.* 20 (2020) 765–776.
- M.E. Germain, M.J. Knapp, Optical explosives detection: from color changes to fluorescence turn-on, *Chem. Soc. Rev.* 38 (2009) 2543–2555.
- M.J. Lefferts, M.R. Castell, Vapour sensing of explosive materials, *Anal. Methods* 7 (2015) 9005–9017.
- X. Sun, Y. Wang, Y. Lei, Fluorescence based explosive detection: from mechanisms to sensory materials, *Chem. Soc. Rev.* 44 (2015) 8019–8061.
- C. Li, X. Yang, J.C. Yu, T. Ming, J. Wang, Porous upconversion materials-assisted near infrared energy harvesting by chlorophylls, *Chem. Commun.* 47 (2011) 3511–3513.
- C. Zhang, Y. Che, Z. Zhang, X. Yang, L. Zang, Fluorescent nanoscale zinc(II)-carboxylate coordination polymers for explosive sensing, *Chem. Commun.* 47 (2011) 2336–2338.
- Z.u. Nisa, L. Tashi, C. Sen, N.A. Ashashi, S.C. Sahoo, H.N. Sheikh, Synthesis of eight isostructural 2D lanthanide coordination polymers assembled by rigid furan-2,5-dicarboxylic acid and flexible adipic acid as linkers and exploration of luminescent Eu/Tb polymers as efficient and sensitive sensors for nitroaromatic compounds, *New J. Chem.* 44 (2020) 8125–8137.
- D.E. Barry, D.F. Caffrey, T. Gunnlaugsson, Lanthanide-directed synthesis of luminescent self-assembly supramolecular structures and mechanically bonded systems from acyclic coordinating organic ligands, *Chem. Soc. Rev.* 45 (2016) 3244–3274.
- J.-K. Wang, X.-W. Wang, Z.-S. Wang, L.-S. Yao, L.-Z. Niu, Y.-H. Yu, J.-S. Gao, Two zinc coordination polymers constructed by 4'-hydroxy-[1,1'-biphenyl]-3,5-dicarboxylic acid (H2BDA) and 4-hydroxy-[1,1'-biphenyl]-3,3',5,5'-tetracarboxylic acid (H3BTA): Synthesis, structures and luminescence identifying properties, *Polyhedron* 167 (2019) 85–92.
- X.-T. Zhang, H.-T. Chen, B. Li, G.-Z. Liu, X.-Z. Liu, 3-Fold and 6-Fold interpenetrating diamond nets based on the designed N, N'-dioxide 3,3'-benzo(c)cinoline dicarboxylic acid with highly sensitive luminescence sensing for NACs and  $\text{Fe}^{3+}$  ion, *J. Solid State Chem.* 267 (2018) 28–34.
- M. Abudourehman, L. Wang, X. Zhang, H. Yu, Z. Yang, C. Lei, J. Han, S. Pan,  $\text{Pb}_3\text{O}(\text{OH})_3(\text{CO}_3)_3(\text{BO}_3)$ : first mixed borate and carbonate nonlinear optical material exhibiting large second-harmonic generation response, *Inorg. Chem.* 54 (2015) 4138–4142.
- D. Sun, F.J. Liu, R.B. Huang, L.S. Zheng, Anionic heptadecanuclear silver(I) cluster constructed from in situ generated 2-mercaptopbenzoic acid and a sulfide anion, *Inorg. Chem.* 50 (2011) 12393–12395.
- D.F. Sun, Y.X. Ke, D.J. Collins, G.A. Lorigan, H.-C. Zhou, Construction of robust open metal – organic frameworks with chiral channels and permanent porosity, *Inorg. Chem.* 46 (2007) 2725–2734.
- X.T. Zhang, H.T. Chen, B. Li, G.Z. Liu, X.Z. Liu, Construction of functional coordination polymers derived from designed flexible bis(4-carboxybenzyl)amine, *CrystEngComm* 21 (2019) 1231–1241.
- X.Q. Wang, J. Yang, L.L. Zhang, F.L. Liu, F.N. Dai, D.F. Sun, Synthesis of two triarylboron-functionalized metal-organic frameworks: in situ decarboxylic reaction, structure, photoluminescence, and gas adsorption properties, *Inorg. Chem.* 53 (2014) 11206–11212.
- H.Q. Ma, D. Sun, L.L. Zhang, R.M. Wang, V.A. Blatov, J. Guo, D.F. Sun, A “strongly” self-catenated metal-organic framework with the highest topological density among 3,4-coordinated nets, *Inorg. Chem.* 52 (2013) 10732–10734.
- Z. Xiao, M. Zhang, W. Fan, Y. Qian, Z. Yang, B. Xu, Z. Kang, R. Wang, D. Sun, Highly efficient oil/water separation and trace organic contaminants removal based on superhydrophobic conjugated microporous polymer coated devices, *Chem. Eng. J.* 326 (2017) 640–646.
- Z. Xiao, P. Liu, J. Zhang, H. Qi, J. Liu, B. Li, X. Sun, Q. Zhang, C. Wei, L. Wang, Pillar-coordinated strategy to modulate phase transfer of  $\alpha\text{-Ni}(\text{OH})_2$  for enhanced supercapacitor application, *ACS Appl. Energy Mater.* 3 (2020) 5628–5636.
- Z. Xiao, Y. Wang, B. Xu, S. Du, W. Fan, D. Cao, Y. Deng, L. Zhang, L. Wang, D. Sun, An integrated chemiluminescence microreactor for ultrastrong and long-lasting light emission, *Adv. Sci.* 7 (2020) 2000065–2000070.
- Y. Rachuri, B. Parmar, K.K. Bisht, E. Suresh, Structural studies and detection of nitroaromatics by luminescent 2D coordination polymers with angular dicarboxylate ligands, *Inorg. Chem. Front.* 2 (2015) 228–236.
- J.F. Zhang, B. Xu, F.M. Luo, G.D. Tang, C. Zhang, Two 4'-(4-carboxyphenyl)-3,2':6',3'-terpyridine-based luminescent Zn(II) coordination polymers for detection of 2,4,6-trinitrophenol, *Polyhedron* 169 (2019) 51–57.



[首页](#) [我的科研](#)

当前位置 - 我的科研 - 我的项目 - 已立项项目

[返回](#)

立项信息    项目成员    到账经费    支出经费    年度经费    变更结题情况    经费预算    经费执行情况

## 【项目基本信息】

校内编号 *	1910400002MZ
项目编号	201803D221026-4
项目名称 *	基于肠道菌群多样性原理研发替代抗生素的饲料添加剂及其产业化示范
项目性质	纵向 <input checked="" type="checkbox"/>

## 【项目详细信息】

项目来源 *	山西省科技厅 <input checked="" type="checkbox"/>	项目类别 *	省重点研发计划 (农业领域) <input checked="" type="checkbox"/>
项目级别	一般项目 <input checked="" type="checkbox"/>	项目等级	-请选择- <input checked="" type="checkbox"/>
预期成果形式			
负责人 *	王海宾	学历	博士研究生 <input checked="" type="checkbox"/>
职称	副教授 <input checked="" type="checkbox"/>	承担部门 *	化学工程与技术学院
手机	18234162468 (如:1599****567)	电子邮件	(如:aa@163.com)
学科门类 *	理工类 <input checked="" type="checkbox"/>	二级分类	理科类 <input checked="" type="checkbox"/>
学科分类	-请选择- <input checked="" type="checkbox"/>		
项目密级	-请选择- <input checked="" type="checkbox"/>	研究类别	-请选择- <input checked="" type="checkbox"/>
社会经济目标	-请选择- <input checked="" type="checkbox"/>	服务国民经济行业	-请选择- <input checked="" type="checkbox"/>
合同编号			
合同开始日期 *	2018-04-01	合同完成日期 *	2020-12-31
立项日期 *	2019-01-11		
研究期限			
是否合作项目 *	<input checked="" type="radio"/> 是 <input type="radio"/> 否	学校排名	1
合作形式	技术服务 <input checked="" type="checkbox"/>		
立项文件文号			
归档状态	未归档	归档日期	

## 【项目承担单位】

署名顺序	单位名称	省份/国家	地市、区县	联系人	联系人电话、手机
2	大禹生物工程有限公司	山西	运城、芮城县	麻啸涛	18636300040

## 【项目经费信息】

申请经费(万元)	30.0000	合同总经费(万元) *	10.0000
下拨经费(万元)		财政经费(万元)	
企业自筹经费(万元)		个人自筹经费(万元)	
配套经费(万元)		地方配套经费(万元)	
校内配套(万元)		应到校经费(万元)	
管理费(万元)		项目可用经费总额(万元)	
经费帐号	1910400002MZ		

## 【上传附件】

申请书附件 [提交4](#)



- [34] Y. Zhang, Q.F. Yang, X.P. Li, C.X. Miao, Q. Hou, S.Y. Ai, A Cu(I)-I coordination polymer fluorescent chemosensor with amino-rich sites for nitro aromatic compound (NAC) detection in water, *CrystEngComm*. 22 (2020) 5690–5697.
- [35] A.K. Ghosh, A. Hazra, A. Mondal, P. Banerjee, Weak interactions: The architect behind the structural diversity of coordination polymer, *Inorg. Chim. Acta*. 488 (2019) 86–119.
- [36] X.-L. Wan, L. Dong, J.-Z. Wang, H.-T. Shi, L.-B. Yang, Synthesis, structure and in vitro anti-gastric cancer activity of two new mixed-ligand Cu(II) and Cd(II)-coordination polymers, *J. Inorg. Organomet. Polym. Mater.* 29 (2019) 1184–1191.
- [37] D. Sun, M.Z. Xu, S.S. Liu, S. Yuan, H.F. Lu, S.Y. Feng, D.F. Sun, Eight Zn (II) coordination networks based on flexible 1,4-di(1H-imidazol-1-yl) butane and different dicarboxylates: crystal structures, water clusters, and topologies, *Dalton Trans.* 42 (2013) 12324–12333.
- [38] X.Q. Wang, D.D. Feng, J. Tang, Y.D. Zhao, J. Li, J. Yang, C.K. Kim, F. Su, A water-stable zinc(ii)-organic framework as a multiresponsive luminescent sensor for toxic heavy metal cations, oxyanions and organochlorine pesticides in aqueous solution, *Dalton Trans.* 48 (2019) 16776–16785.
- [39] J. Sun, K.-X. Shang, Y.-J. Wu, Q. Zhang, X.-Q. Yao, Y.-X. Yang, D.-C. Hu, J.-C. Liu, Three new Coordination Polymers based on a 1-(3,5-dicarboxy-benzyl)-1H-pyrazole-3,5-dicarboxylic acid ligand: Synthesis, crystal structures, magnetic properties and selectively sensing properties, *Polyhedron*. 141 (2018) 223–229.
- [40] Z. Xiao, X. Yang, S. Zhao, D. Wang, Y. Yang, L. Wang, Metal–organic hybrid materials built with tetrachlorophthalate acid and different N-donor coligands: Structure diversity and photoluminescence, *J. Solid State Chem.* 234 (2016) 36–47.
- [41] S.H. Zhang, S.Y. Zhang, J.R. Li, Z.Q. Huang, J. Yang, K.F. Yue, Y.Y. Wang, Rational synthesis of an ultra-stable Zn(ii) coordination polymer based on a new tripodal pyrazole ligand for the highly sensitive and selective detection of  $\text{Fe}^{3+}$  and  $\text{Cr}_2\text{O}_7^{2-}$  in aqueous media, *Dalton Trans.* 49 (2020) 11201–11208.
- [42] J. Wang, Y. Zhong, C. Bai, Y. Guan, Y. Pan, H.-M. Hu, Series of coordination polymers with multifunctional properties for nitroaromatic compounds and CuII sensing, *J. Solid State Chem.* 288 (2020) 121381–121391.
- [43] Y.J. Zhang, D.S. Zhao, Z.J. Liu, J.D. Yang, X.Y. Niu, L.M. Fan, T.P. Hu, Synthesis of two isostructural Zn-CPs and their fluorescence sensing for Cr (VI) ion and nitrofurantoin in aqueous medium, *J. Solid State Chem.* 282 (2020) 121086–121090.
- [44] J. Buasakun, P. Srilaong, K. Chainok, C. Raksakoon, R. Rattanakram, T. Duangthongyou, Novel zinc(II) coordination polymers (CPs) based on flexible aliphatic carboxylic acids and an N-donor ligand for fluorescence sensors, *Inorg. Chim. Acta*. 511 (2020) 119839–119852.
- [45] X. Zhou, Y.-X. Shi, C. Cao, C.-Y. Ni, Z.-G. Ren, D.J. Young, J.-P. Lang, Nickel(II)-based two-dimensional coordination polymer displaying superior capabilities for selective sensing of Cr(VI) ions in water, *Cryst. Growth Des.* 19 (2019) 3518–3528.
- [46] C.B. Fan, L.L. Wang, C.G. Xu, R.X. Wu, N.N. Li, D.M. Zhang, X. Zhang, S.Y. Bi, Y. H. Fan, Synthesis, structure diversity, and dye adsorption and luminescent sensing properties of Zinc (II) coordination polymers based on 1,3,5-tris(1-imidazolyl) benzene and 1,3-bis(1-imidazolyl)toluene, *J. Solid State Chem.* 288 (2020) 121445–121453.
- [47] M.-M. Fu, Y.-H. Qu, V.A. Blatov, Y.-H. Li, G.-H. Cui, Two d10 metal coordination polymers as dual functional luminescent probes for sensing of  $\text{Fe}^{3+}$  ions and acetylacetone with high selectivity and sensitivity, *J. Solid State Chem.* 289 (2020) 121460–121468.
- [48] F.F. Li, M.L. Zhu, L.P. Lu, A luminescent Cd(II)-based metal–organic framework for detection of Fe(III) ions in aqueous solution, *J. Solid State Chem.* 261 (2018) 31–36.
- [49] L. Li, J.Y. Zou, S.Y. You, H.M. Cui, G.P. Zeng, J.Z. Cui, Tuning the luminescence of two 3d–4f metal–organic frameworks for the fast response and highly selective detection of aniline, *Dalton Trans.* 46 (2017) 16432–16438.
- [50] Y.J. Zhang, L.L. Gao, J. Zhang, H.N. Wu, L.M. Fan, T.P. Hu, Structural diversity, magnetic properties, and luminescent sensing of four coordination polymers based on 6-(3,5-dicarboxylphenyl)nicotinic acid, *J. Solid State Chem.* 271 (2019) 40–46.
- [51] Y.J. Zhang, J.D. Yang, D.S. Zhao, Z.J. Liu, D.C. Li, L.M. Fan, T.P. Hu, Two cadmium (ii) coordination polymers as luminescent sensors for the detection of nitrofurantoin/nitroimidazole antibiotics, *CrystEngComm*. 21 (2019) 6130–6135.



Cite this: *CrystEngComm*, 2021, 23, 2862

# Ni-Co LDH/M-Mo-S (M = Zn, Co and Ni) nanoarrays as efficient water oxidation electrocatalytic materials†

Haibin Wang<sup>a</sup> and Xiaoshuang Zhang<sup>\*b</sup>

It is possible to research the influencing factors of the electrocatalytic water splitting activity by controlling the composition and morphology of the materials. In this study, an efficient morphology control of Ni-Co layered double hydroxide/M-Mo-S (M = Zn, Co and Ni) hybrid materials was investigated by introducing different metal ions into M-Mo-S. An adjustable morphology was successfully achieved by taking the advantage of the growth mechanism of the Kirkendall growth and Ostwald ripening. The Ni-Co LDH/Ni-Mo-S catalyst displayed an extraordinary oxygen evolution reaction performance (overpotential of 290 mV at 40 mA cm<sup>-2</sup>) and a superior durability (retention rate of 90%) at 10 mA cm<sup>-2</sup> after 14 h compared to Ni-Co LDH/M-Mo-S (M = Zn, Co and Ni) hybrid materials. A series of characterization analyses demonstrate that the efficient electrochemistry performance of the material is assigned to the improved electrical conductivity, greater exposure to active sites and faster oxygen outflow rate. The density functional theory calculation results suggest that the *in situ* generated Mo-doped NiOOH has the optimal adsorption energy of water compared to NiOOH, which is probably the main active center in the water oxidation reaction. Our study presents a new way of thinking for the development of high efficiency heterojunction catalysts and guidance for the further realization of the industrialization of electrolytic water.

Received 19th February 2021,  
Accepted 14th March 2021

DOI: 10.1039/d1ce00247c

rsc.li/crystengcomm

## 1. Introduction

The growing energy crisis and increasingly severe environmental pollution force us to develop new zero carbon and pollution-free energy. Hydrogen has attracted wide public attention because of its high combustion value, high energy density and pollution-free combustion products. It is worth noting that water electrolysis to hydrogen is considered as one of the most fascinating alternatives to traditional coal chemical engineering due to its simple equipment and high purity hydrogen production.<sup>1–3</sup> Electrocatalytic water electrolysis consists of two and a half reactions, namely oxygen evolution reaction (OER) at the anode and hydrogen evolution reaction (HER) at the cathode. The electrocatalytic water splitting into hydrogen and oxygen is accomplished through electricity, which is generated by solar energy or waste electricity. In the whole water electrolysis reaction, oxygen evolution reaction has become the bottleneck of water electrolysis because it contains the kinetic obstruction of

multiple electrons and protons. Therefore, it is very important to develop relatively inexpensive, robust and environmentally friendly water oxidation catalysts. According to literature reports,<sup>4–11</sup> the most active water oxidation catalysts at present are the materials containing precious metals, such as RuO<sub>2</sub> and IrO<sub>2</sub>. However, their scarcity, instability and high price greatly limit their application in industrial production for water splitting.<sup>12–26</sup> Therefore, the exploitation of efficient, relatively inexpensive and stable oxygen evolution reaction electrode is both an opportunity and a challenge.<sup>27–30</sup>

To date, metal oxides have been developed as electrodes for the electrolysis of water, but their poor electrical conductivity greatly limits their practical application. Recently, layered double hydroxides (LDHs) and transition metal sulfides (TMSs) have been exploited as promising water splitting materials owing to their excellent electroconductibility and electrocatalytic activity compared to binary metal oxides. It is worth mentioning that bimetallic LDHs and transition metal sulfides provide more redox sites and greater specific surface area, leading to superior electrocatalytic water electrolysis activity. For example, Wei *et al.*<sup>31</sup> reported the synthesis of CoMoS<sub>4</sub> nanoarrays on carbon cloth by the sulfidizing processing of Co(OH)F in an (NH<sub>4</sub>)<sub>2</sub>MoS<sub>4</sub> solution. The CoMoS<sub>4</sub> nanoarrays exhibit superior electrocatalytic performance in a neutral buffer solution with an overpotential of 183 mV to obtain 10 mA

<sup>a</sup> School of Chemical Engineering and Technology, North University of China, Taiyuan 030051, People's Republic of China

<sup>b</sup> School of Science, North University of China, Taiyuan, P. R. China.  
E-mail: 20160068@nuc.edu.cn

† Electronic supplementary information (ESI) available. See DOI: 10.1039/d1ce00247c

$\text{cm}^{-2}$  as a HER material. Fichou *et al.*<sup>32</sup> reported the synthesis and electrochemistry activity of porous  $\text{CoMo}_2\text{S}_4$  nanoflake materials. The  $\text{CoMo}_2\text{S}_4$  sample presents better electrochemistry activity with the need of a small OER/HER overpotential of 306/162 mV to drive  $10 \text{ mA cm}^{-2}$ . Moreover, Lee *et al.*<sup>33</sup> reported the synthesis of Ni-Co LDH/ $\text{MMoS}_x$  ( $M = \text{Zn, Co and Ni}$ ) heterogeneous materials, and the Ni-Co LDH/ $\text{NiMoS}_x$  sample displayed a superior specific capacity and a satisfactory cycling stability. However, the previously reported water splitting catalysts are still far from the industrial production of hydrogen so far. This problem is caused by the inadequate utilization of the surface active centers of the materials and the slow electron transfer rate. Therefore, the successful development of highly efficient water splitting catalysts not only increases exposure to active sites of materials but also increases charge transfer capacity. In addition, the resistance can be reduced and the bubble overflow rate can be promoted when the material is *in situ* grown on the conductive substrate during the electrocatalytic process. Hence, loading functional electrocatalysts with refined morphology controlling and suitable exploiting on a conductive frame greatly promotes the electrocatalytic activity of water splitting catalysts.

In the study, for the first time, the morphology of Ni-Co LDH/ $M\text{-Mo-S}$  ( $M = \text{Zn, Co and Ni}$ ) hybrid materials was successfully regulated by taking advantage of the growth mechanism of the Kirkendall effect, ion exchange reaction and Ostwald ripening. The Ni-Co LDH/ $M\text{-Mo-S}$  ( $M = \text{Zn, Co and Ni}$ ) hybrid samples present following four superiorities: (i) when the material is *in situ* grown on the conductive substrate, the resistance can be reduced and the bubble overflow rate can be promoted during the electrocatalytic process; (ii) precise control and reasonable design of the morphology of water splitting electrodes not only increase exposure to active sites of materials but also increase charge transfer capacity, thus promoting the water splitting performance; (iii) these hybrid electrode samples boost the synergistic catalytic effect and improve the water oxidation performance of the catalyst; and (iv) the design of heterogeneous structures effectively accelerates the rate of charge transfer and increases both the electrocatalytic performance and reaction kinetics of the water oxidation reaction. The precise control and reasonable design of Ni-Co LDH/ $\text{Ni-Mo-S}$  hybrid materials are helpful to improve the water oxidation reaction performance (overpotential of 290 mV at  $40 \text{ mA cm}^{-2}$ ) and excellent durability (retention rate of 90%) at  $10 \text{ mA cm}^{-2}$  after 14 h.

## 2. Experimental section

### Preparation of the Ni-Co LDH/ $M\text{-Mo-S}$ ( $M = \text{Co, Ni and Zn}$ ) nanoarray on Ni foam

For the preparation of Ni-Co LDH/ $\text{Co-Mo-S}$  nanoarrays on Ni foam,  $\text{Co}(\text{NO}_3)_2 \cdot 6\text{H}_2\text{O}$  (0.5 mmol),  $\text{Na}_2\text{MoO}_4 \cdot 2\text{H}_2\text{O}$  (0.5 mmol) and  $\text{CH}_3\text{CSNH}_2$  (1.5 mmol) were dissolved in a beaker containing ultrapure water (80 mL) and stirred vigorously.

Then, the solution was poured into an autoclave and a piece of pre-treated Ni foam was vertically inserted into the autoclave. The reaction was kept at  $110^\circ\text{C}$  for 3 h. The reaction was naturally cooled to room temperature and the resulting Ni-Co LDH/ $\text{Co-Mo-S}$  product was washed with water. Ni-Co LDH/ $\text{Ni-Mo-S}$  and Ni-Co LDH/ $\text{Zn-Mo-S}$  nanoarrays were obtained *via* the similar process except replacing  $\text{Co}(\text{NO}_3)_2 \cdot 6\text{H}_2\text{O}$  with  $\text{Ni}(\text{NO}_3)_2 \cdot 6\text{H}_2\text{O}$  (0.5 mmol) and  $\text{Zn}(\text{NO}_3)_2 \cdot 6\text{H}_2\text{O}$  (0.5 mmol), respectively.

## 3. Results and discussion

During the synthesis of Ni-Co LDH/ $M\text{-Mo-S}$  ( $M = \text{Zn, Co and Ni}$ ),  $\text{Na}_2\text{MoO}_4 \cdot 2\text{H}_2\text{O}$  provided a molybdenum source,  $\text{CH}_3\text{-CSNH}_2$  released  $\text{S}^{2-}$  ions constantly into the mixture through hydrolysis, and the  $\text{S}^{2-}$  ions readily got exchanged with the  $\text{OH}^-$  ions of the Ni-Co LDH surface, leading to the generation of thin layers of Ni-Co-S on the outside surface of Ni-Co LDH. In addition, differently controllable structures of Ni-Co LDH/ $M\text{-Mo-S}$  ( $M = \text{Zn, Co and Ni}$ ) hybrid materials can be understood according to ion exchange, the Kirkendall effect and Ostwald ripening. The essence of the Kirkendall effect is the cation exchange between the outer surface and the inner surface of the material, and *vice versa*. Ostwald ripening reveals the formation of hybrid construction over time by dissolving the smaller precipitates inside and reconstructing the structure on the outer surface of a larger precipitate. By regulating and controlling the mixed metal sulfide composition, the structure tuning of resulting samples was possible, which can have a large impact on its electrocatalytic activity. The Ni-Co LDH and Ni-Co LDH/ $M\text{-Mo-S}$  ( $M = \text{Zn, Co and Ni}$ ) electrodes display three obvious diffraction peaks at  $43.9^\circ$ ,  $52.1^\circ$  and  $76.1^\circ$ , respectively, corresponding to the characteristic peaks of the Ni foam substrate. The X-ray diffraction images of Ni-Co LDH display five strong peaks at  $18.9^\circ$ ,  $32.9^\circ$ ,  $39.0^\circ$ ,  $58.9^\circ$  and  $63.2^\circ$ , respectively, which are assigned to the (001), (100), (011), (110) and (111) diffraction

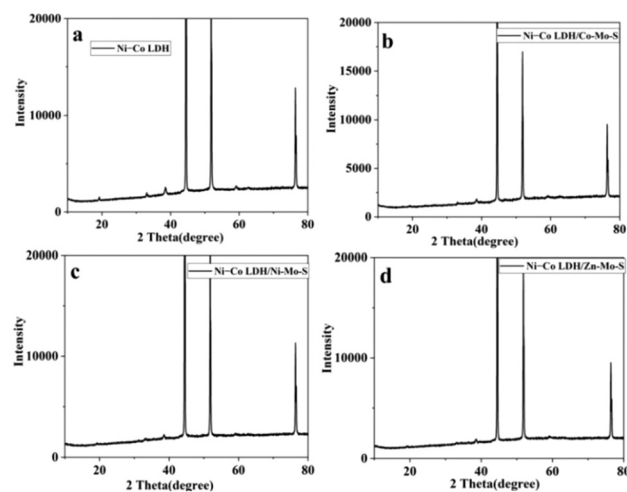


Fig. 1 XRD of Ni-Co LDH (a), Ni-Co LDH/ $\text{Co-Mo-S}$  (b), Ni-Co LDH/ $\text{Ni-Mo-S}$  (c) and Ni-Co LDH/ $\text{Zn-Mo-S}$  (d).

crystal planes of  $\text{Ni}(\text{OH})_2$  (JCPDS no. 73-1520) and  $\beta\text{-Co}(\text{OH})_2$  (JCPDS no. 30-0443) (Fig. 1a). It is worth noting that the XRD patterns of Ni-Co LDH/M-Mo-S (M = Zn, Co and Ni) materials are similar to those of the Ni-Co LDH material, and no apparent diffraction peaks of M-Mo-S (M = Zn, Co and Ni) were observed. The possible reason is that the loading amount of Ni-Co LDH/M-Mo-S (M = Zn, Co and Ni) is about 2–3 mg on the Ni foam, which may be beyond the detection limit for Ni-Co LDH/M-Mo-S (M = Zn, Co and Ni) materials. It is noteworthy to mention that the diffraction intensity of Ni-Co LDH/M-Mo-S (M = Zn, Co and Ni) significantly reduced compared to that of Ni-Co LDH (Fig. 1b–d), which also proves the existence of M-Mo-S (M = Zn, Co and Ni). We tried to scrape the catalyst off the Ni foam, but we were not successful because the amount was too small. The Raman signal is also almost unobservable, and this kind of phenomenon further indicates that the material load is small (Fig. S1†).

The morphology of the catalyst also affects the electrocatalytic performance of the material to a great extent. The SEM analysis was first performed based on the above-mentioned reasons. Fig. 2a–h display the hetero

nanostructures of Ni-Co LDH/M-Mo-S (M = Zn, Co and Ni) materials. Fig. 2a and b indicate that one-dimensional nanorod and two-dimensional nanosheet architecture for the Ni-Co LDH material formed with the irregular length and size. The SEM image of Ni-Co LDH/Co-Mo-S displays a flaky-spherical hybrid structure (Fig. 2c and d), and the diameter of each nano spherical was measured to be around 100 nm. For the Ni-Co LDH/Ni-Mo-S material, the one-dimensional nanorod and two-dimensional nanosheet architecture microstructure of Ni-Co LDH are kept due to the growth mechanism of Kirkendall growth and Ostwald ripening (Fig. 2e and f). The thickness of the Ni-Mo-S shell is observed to be around 500 nm. The hierarchical architecture of the one-dimensional nanorod and two-dimensional nanosheet architectures promotes the transmission and diffusion of the electrolyte and increases the active site of the catalyst, thereby leading to a rapid charge transfer rate and enhanced electrochemistry activity of the electrode. In the case of the Ni-Co LDH/Zn-Mo-S material, the flaky-spherical hybrid structure of the material is maintained (Fig. 2g–h) and the diameter of the Co-Mo-S shell is observed to be around 50 nm. The Ni-Co LDH/Ni-Mo-S material displays superior electrocatalytic performances because of the one-dimensional nanorod architecture of Ni-Co LDH together with a thinner nanosheet of Ni-Mo-S compared to Ni-Co LDH/M-Mo-S (M = Zn, Co and Ni) materials.

Transmission electron microscopy (TEM) was done to further investigate the morphology and composition of the Ni-Co LDH/Ni-Mo-S sample. It can be seen from Fig. 3a that the Ni-Co LDH/Ni-Mo-S electrode displays the core-shell structure of nanorods, which is consistent with the characterization analysis of SEM. The lattice fringe and

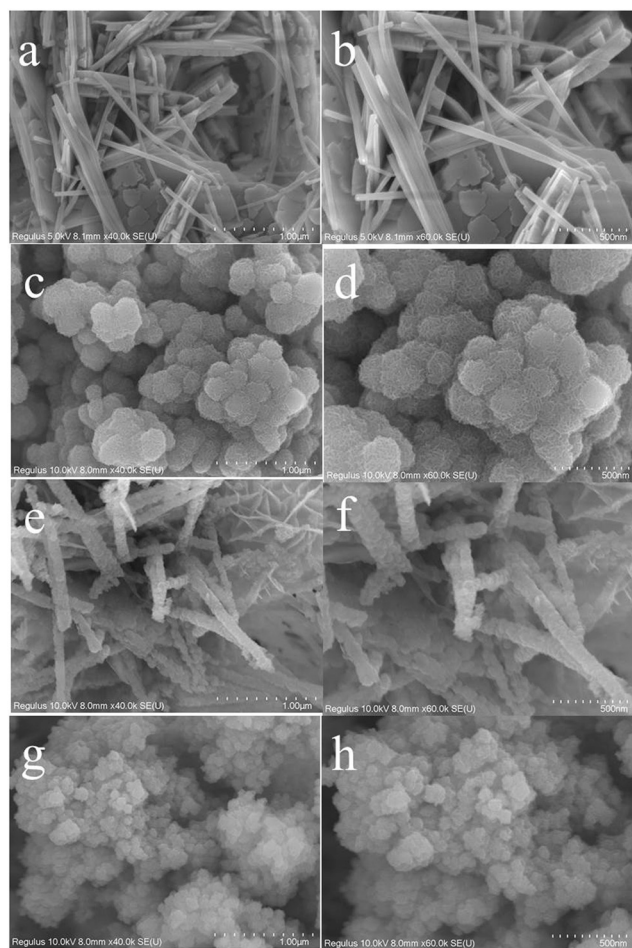


**Fig. 2** SEM of the Ni-Co LDH material (a and b), Ni-Co LDH/Co-Mo-S (c and d), Ni-Co LDH/Ni-Mo-S (e and f), Ni-Co LDH/Zn-Mo-S (g and h).

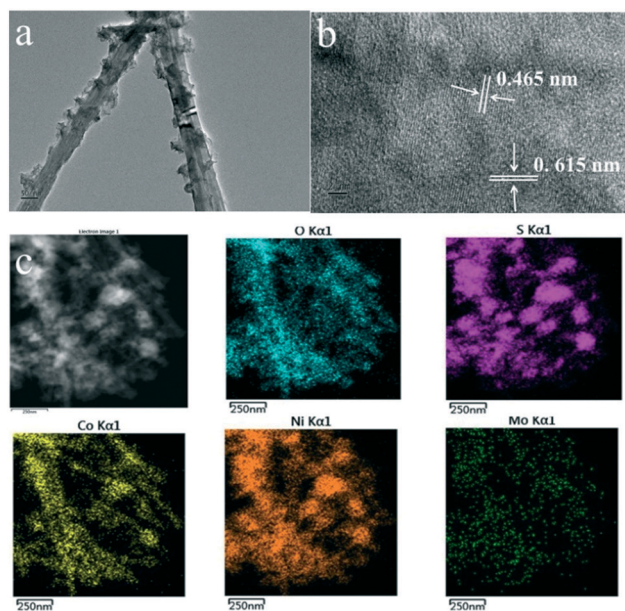


**Fig. 3** TEM (a), HR-TEM images (b) and corresponding EDS element mapping of Ni-Co LDH/Ni-Mo-S/NF (c).



microstructure of the Ni-Co LDH/Ni-Mo-S material were also investigated *via* high resolution TEM (HR-TEM). The lattice spacings of the electrode are 0.465 nm and 0.615 nm, corresponding to the (001) and (002) plane spacings of Ni-Co LDH and MoS<sub>2</sub> (Fig. 3b). The corresponding EDS elemental mapping results (Fig. 3c) suggest that Ni, Co, Mo, S and O are evenly distributed in the resulting Ni-Co LDH/Ni-Mo-S material.

X-ray photoelectron spectroscopy (XPS) is an excellent detection method for getting a deeper insight into the microscopic properties and valence states of the Ni-Co LDH/M-Mo-S (M = Zn, Co and Ni) material surface. The XPS full scan spectrum of Ni-Co LDH/Ni-Mo-S displays the presence of Ni, Co, Mo, O and S elements (Fig. 4a). The high-resolution spectra of Ni 2p and Co 2p (Fig. 4b and c) split into two main peaks accompanied by two shakeup satellites. The low binding energy at about 855.5 and 857.2 eV and the high binding energy at around 873.7 and 876.6 eV correspond to the Ni 2p<sub>3/2</sub> and Ni 2p<sub>1/2</sub> of the Ni 2p spectrum, respectively (Fig. 4b). The two shakeup peaks at around 862.3 and 879.9 eV are assigned to the satellite peaks of the Ni oxidation state ions. In addition, the low binding energy at about 781.5 eV and the high binding energy at about 797.5 eV correspond to the Co 2p<sub>3/2</sub> and Co 2p<sub>1/2</sub> of the Co 2p spectrum (Fig. 4c). The two shakeup peaks at about 784.3 and 803.2 eV are assigned to the satellite peaks of the Co oxidation state ions. The experimental analysis demonstrates the presence of the Ni oxidation state and Co oxidation state ions in the Ni-Co LDH/Ni-Mo-S material. The high-

resolution Mo 3d spectrum presents two peaks: one peak at about 232.1 eV is assigned to Mo 3d<sub>5/2</sub> (Fig. 4d) and the other peak at about 235.5 eV corresponds to Mo 3d<sub>3/2</sub> of Ni-Mo-S, suggesting the existence of Mo<sup>6+</sup> ions. The O 1s spectrum splits into two main peaks (Fig. 4e): one peak at 531.7 eV is assigned to the M-O of Ni-Co LDH and the other peak at about 533.5 eV corresponds to the adsorbed oxygen species for the Ni-Co LDH/Ni-Mo-S material. It can be seen from Fig. 4f that the binding energies of two peaks at about 161.9 and 164.0 eV correspond to S 2p<sub>3/2</sub> and S 2p<sub>1/2</sub> of Ni-Mo-S for the S 2p spectrum. Another peak at around 169.0 eV is indexed to oxidized sulfur on the Ni-Mo-S surface. These XPS characterization analyses demonstrate that Co<sup>2+</sup>, Co<sup>3+</sup>, Ni<sup>2+</sup>, Ni<sup>3+</sup>, Mo<sup>6+</sup>, O<sup>2-</sup> and S<sup>2-</sup> exist in the Ni-Co LDH/Ni-Mo-S material.

The electrocatalytic performance of the Ni-Co LDH/M-Mo-S (M = Zn, Co and Ni) material was investigated on a typical three-electrode system in an alkaline medium. As shown in Fig. 5a, the Ni-Co LDH/Ni-Mo-S material displays the superior OER electrocatalytic performance (Table 1) compared to Ni-Co LDH and Ni foam (Fig. S2†). It is noteworthy to mention that different metal ions will greatly affect the electrochemistry activity of the materials. From Fig. 5a, a distinct oxidation peak can be observed, which is attributed to Ni<sup>2+</sup> to Ni<sup>3+</sup> oxidation. It is important to note that the increase in the first peak current may be assigned to the capacitance of the material at 1.2–1.4 V. The increase in the second peak current after 1.45 V is caused by the water splitting for Ni-Co LDH/M-Mo-S (M = Zn, Co and Ni). The Tafel slope of materials was also explored to research the rate of electron transfer in the reaction. The Tafel slope of Ni-Co LDH/Ni-Mo-S has a comparatively low value of 116.6 mV dec<sup>-1</sup>, which is smaller than those of Ni-Co LDH/Zn-Mo-S (127.8 mV dec<sup>-1</sup>), Ni-Co LDH/Co-Mo-S (131.2 mV dec<sup>-1</sup>) and

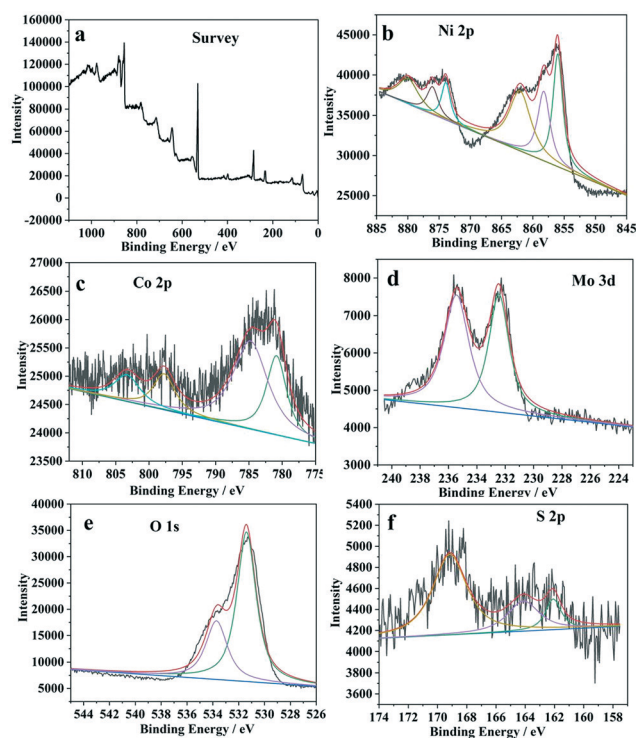


Fig. 4 XPS of the Ni-Co LDH/Ni-Mo-S, survey (a), Ni 2p (b), Co2p (c), Mo 3d (d), O 1s (e) and S 2p (f).

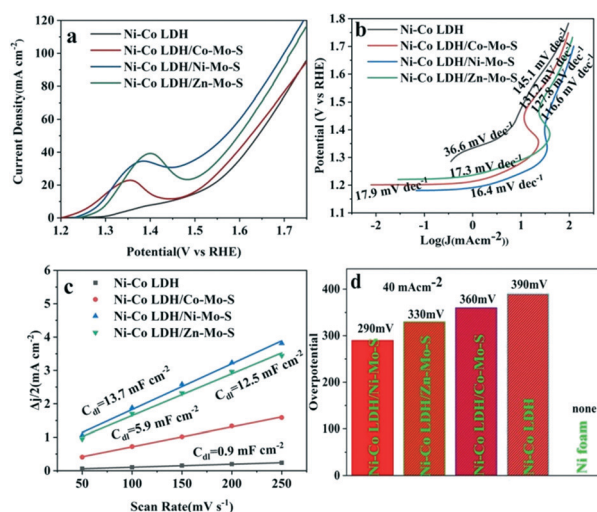


Fig. 5 (a) OER curves of the Ni-Co LDH/M-Mo-S (M = Zn, Co and Ni) materials. (b) Tafel plots of the Ni-Co LDH/M-Mo-S (M = Zn, Co and Ni) sample. (c) The double layer capacitance of the Ni-Co LDH/M-Mo-S (M = Zn, Co and Ni) material. (d) The overpotential of the Ni-Co LDH/M-Mo-S (M = Zn, Co and Ni) sample.

**Table 1** Comparison of the water oxidation activity between the Ni-Co LDH/Ni-Mo-S and other recently reported water oxidation electrocatalysts

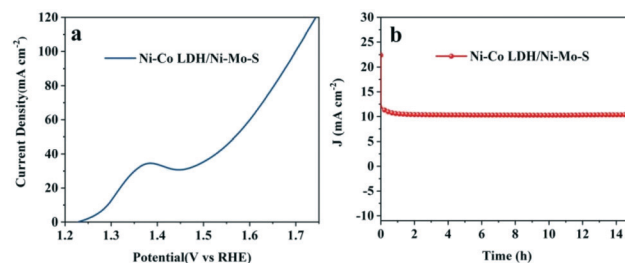
Catalyst	Overpotential ( $j = 10 \text{ mA cm}^{-2}$ )	Ref.
Ni-Co LDH/Ni-Mo-S	290 mV@40 mA cm <sup>-2</sup>	This study
O-CoP	310 mV	34
Se-MnS/NiS	211 mV	35
(Ni,Co) <sub>0.85</sub> Se@NiCo-LDH	216 mV	36
Ni <sub>x</sub> Fe <sub>1-x</sub> Se <sub>2</sub>	195 mV	37
NiFeP	219 mV	38
NF@NC-CoFe <sub>2</sub> O <sub>4</sub> /C	240 mV	39
CC/CNTs@CoS <sub>0.74</sub> Se <sub>0.52</sub>	285 mV	40
CoMn oxide	221 mV	41
NF/H-CoMoO <sub>4</sub>	295 mV	42
CoSe <sub>2</sub> /FeSe <sub>2</sub>	240 mV	43
CuS/NiS <sub>2</sub>	290 mV	44
NiS <sub>2</sub> /CoS <sub>2</sub>	235 mV	45

Ni-Co LDH (145.1 mV dec<sup>-1</sup>). On the basis of the Tafel slope of Ni-Co LDH/Ni-Mo-S, it can be seen that the Tafel slope of the Ni-Co LDH/Ni-Mo-S hybrid material is 16.4 mV dec<sup>-1</sup> in the potential region of 1.15–1.40 V (Fig. 5b), demonstrating that the oxidation of Ni-Mo-S is a very fast process. This result is assigned to the optimized water adsorption energy to water species and large surface area of the Ni-Co LDH/Ni-Mo-S. In the region 1.40–1.69 V, Ni-Co LDH/Ni-Mo-S displays a higher Tafel slope of 116.6 mV dec<sup>-1</sup>, which indicates that the O=O bond formation is a slow kinetic process. The double-layer capacitances are provided in order to explore the relationship between the catalytic activity and structure. The double-layer capacitance of Ni-Co LDH/Ni-Mo-S (13.7 mF cm<sup>-2</sup>) is larger than that of Ni-Co LDH/Zn-Mo-S (12.5 mF cm<sup>-2</sup>), Ni-Co LDH/Co-Mo-S (5.9 mF cm<sup>-2</sup>) and Ni-Co LDH (0.9 mF cm<sup>-2</sup>), which demonstrates that the Ni-Co LDH/Ni-Mo-S material has more exposure to the active sites (Fig. 5c). It can be seen from Fig. 5d that Ni-Co LDH/Ni-Mo-S also displays the lowest overpotential (290 mV@40 mA cm<sup>-2</sup>) compared to Ni-Co LDH/Zn-Mo-S (330 mV), Ni-Co LDH/Co-Mo-S (360 mV), Ni-Co LDH (390 mV) and RuO<sub>2</sub> (300 mV) (Fig. S4†). Moreover, the Ni-Co LDH/Ni-Mo-S material displays an extremely superior mass activity of 20.5 A g<sup>-1</sup> at an overpotential of 400 mV, which is larger than that of Ni-Co LDH/Co-Mo-S and Ni-Co LDH/Zn-Mo-S. In addition, Faraday efficiency is given to show whether all the produced oxygen is converted from electricity, and further examining the conversion rates between electricity and chemical energy. The experiment characterization suggests that the Ni-Co LDH/Ni-Mo-S electrode presents 95% efficiency for OER (Fig. S5†).

Based on the above analysis, the SEM characterization demonstrates that the hierarchical architecture of the one-dimensional nanorod and two-dimensional nanosheet architectures promotes the transmission and diffusion of the electrolyte and increases the active site of the catalyst, thereby leading to a rapid charge transfer rate and enhanced electrochemistry activity of the electrode. In addition, Ni-Mo-S has superior electronic conductivity and thus reduces

the electrical resistance of the materials while improving the electron transfer rate. The H<sub>2</sub>O molecule is first adsorbed on the interface of Ni-Co LDH and Ni-Mo-S due to the presence of Ni-Mo-S, in which Ni-Co LDH uses as an electron transfer promoter and generates oxygen active centres, which then react with the interface of Ni-Mo-S. Moreover, Ni foam with a porous, higher specific surface area and superior metal properties was used as the current collector, which brings strong electrical connection among the catalyst and conductive substrate. Importantly, 3D texture due to the Ni foam brings high gas diffusivity and easy penetration of the electrolyte and results in better catalysis for the Ni-Co LDH/M-Mo-S (M = Zn, Co and Ni) binder-free materials. Thus, the problems of “dead volume” and slow gas diffusivity are solved, leading to an improvement in the electrocatalytic water oxidation activity. We also researched the durability of the Ni-Co LDH/Ni-Mo-S electrode, and it is found that the current intensity of the Ni-Co LDH/Ni-Mo-S material has no obvious attenuation after 15 h of measurement (Fig. 6a and b). Recently, some electrocatalytic samples are also found to be stable and converted into active species during oxidized conditions. A series of characterization was performed so as to further research the crystal phase, microstructure and active composition of the Ni-Co LDH/Ni-Mo-S material after the reaction. The characterization analysis suggested that the crystal phase and microstructure of the electrode hardly changed appreciably (Fig. S6†). In addition, XPS characterization was performed to study the active composition of materials. It was found that the XPS signals of Ni and Co were almost unchanged before and after the reaction (Fig. S7a–c†). As shown in Fig. S7d and e†, the reduction in the Mo 3d and S 2p signals suggests that the Ni-Co LDH/Ni-Mo-S electrode surface underwent partial oxidation, resulting in the loss of a small amount of Mo and S. However, the electrocatalytic performance of the material will not be affected during the water oxidation process. The change in the oxygen signal (Fig. S7f†) also indicates that amorphous oxides (Mo doped NiOOH) are *in situ* formed on the catalyst surface, which is the real catalytic species.

In the process of water oxidation, the active oxides or hydroxides (NiOOH) will be *in situ* generated on the surface of the material. DFT calculations were performed to estimate the adsorption energy of water on the surfaces of NiOOH and Mo-NiOOH. It is well known that the higher the surface

**Fig. 6** (a) Polarization curve of Ni-Co LDH/Ni-Mo-S. (b) Durability measurement of the Ni-Co LDH/Ni-Mo-S electrodes at 1.40 V.

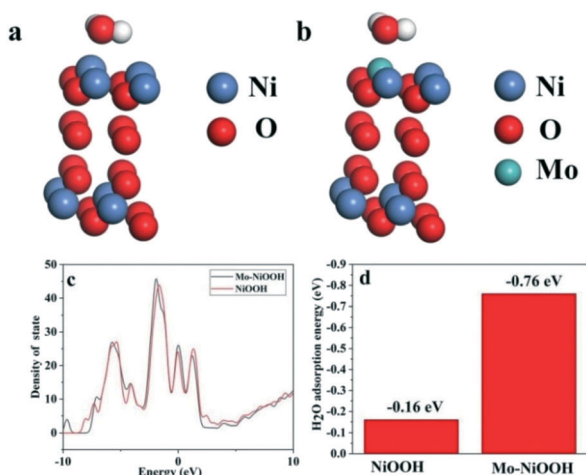


Fig. 7 (a and b) The optimized ball and stick model for water adsorption in NiOOH and Mo-NiOOH. (c) Density of states for NiOOH and Mo-NiOOH. (d) The water adsorption energy for NiOOH and Mo-NiOOH.

adsorption energy of water on the electrode, the higher the catalytic activity of the material. As displayed in Fig. 7a and b, the optimal ball-and-stick model for water adsorption on the catalyst surface is given. As shown in Fig. 7c, the distribution of the state density of Mo-NiOOH near the Fermi level is larger compared to NiOOH, which proves that Mo-NiOOH has good electrical conductivity. It can be seen from Fig. 7d that the water adsorption energy of Mo-NiOOH ( $-0.76$  eV) is significantly greater than that of NiOOH ( $-0.16$  eV), which proves that the greater the water adsorption energy is, the more favorable it is for the water oxidation reaction to occur. In addition, the state density distribution is mainly composed of the p orbital of O and d orbital of Ni for NiOOH (Fig. S8†). The state density distribution is mainly made up of the d orbital of Ni, d orbital of Mo and p orbital of O for Mo-NiOOH (Fig. S9†). The d orbital of Ni overlaps with p orbital of O and the d orbital of Mo overlaps with the p orbital of O, proving the formation of the Ni-O and Mo-O bonds.

## 4. Conclusion

A series of Ni-Co LDH/M-Mo-S ( $M = \text{Zn}, \text{Co}$  and  $\text{Ni}$ ) materials was first prepared taking advantage of the growth mechanism of the Kirkendall effect, ion exchange reaction and Ostwald ripening. The Ni-Co LDH/Ni-Mo-S material presents excellent water oxidation performance (overpotential of  $290 \text{ mV}@40 \text{ mA cm}^{-2}$ ), which is comparable to that of  $\text{RuO}_2$  electrocatalysts containing noble metal (overpotential of  $300 \text{ V}@40 \text{ mA cm}^{-2}$ ). The results of the experiment proved that introducing different metal ions into M-Mo-S affected the electrochemistry activity of the Ni-Co LDH/M-Mo-S ( $M = \text{Zn}, \text{Co}$  and  $\text{Ni}$ ) catalyst. Subsequently, a long time electrochemical activity test suggested that the current intensity of the Ni-Co LDH/Ni-Mo-S electrode has no

obvious attenuation during the stability measurement. XPS characterization results showed that some loss occurred for the active species, but did not cause the degradation of catalytic activity. The DFT calculation results suggest that Mo-NiOOH has the optimal adsorption energy of water compared to NiOOH, which is probably the main active center in the water oxidation reaction. This study fills the gap for the exploitation of low cost and robust hybrid catalysts and offers a novel idea for the realization of hydrogen production from industrial water splitting.

## Conflicts of interest

There are no conflicts to declare.

## Acknowledgements

This work was financially supported by the National Science Foundation of China (Grant No. 21802126).



## Notes and references

- 1 S. Arumugam, G. Pandian and S. Sangaraju, *Adv. Funct. Mater.*, 2016, **26**, 4661–4672.
- 2 B. Chang, J. Yang, Y. Shao, L. Zhang, W. Fan, B. Huang, Y. Wu and X. Hao, *ChemSusChem*, 2018, **11**, 3198–3207.
- 3 M. Chauhan, K. P. Reddy, C. S. Gopinath and S. Deka, *ACS Catal.*, 2017, **7**, 5871–5879.
- 4 Y. Zou, B. Xiao, J.-W. Shi, H. Hao, D. Ma, Y. Lv, G. Sun, J. Li and Y. Cheng, *Electrochim. Acta*, 2020, **348**, 136339.
- 5 X. Zou, Y. Liu, G.-D. Li, Y. Wu, D.-P. Liu, W. Li, H.-W. Li, D. Wang, Y. Zhang and X. Zou, *Adv. Mater.*, 2017, **29**, 1700404.
- 6 J. Wang, X. Ma, F. Qu, A. M. Asiri and X. Sun, *Inorg. Chem.*, 2017, **56**, 1041–1044.
- 7 X. Xiong, C. You, Z. Liu, A. M. Asiri and X. Sun, *ACS Sustainable Chem. Eng.*, 2018, **6**, 2883–2887.
- 8 S. Xu, H. Zhao, T. Li, J. Liang, S. Lu, G. Chen, S. Gao, A. M. Asiri, Q. Wu and X. Sun, *J. Mater. Chem. A*, 2020, **8**, 19729–19745.
- 9 X. Li, R. Zhang, Y. Luo, Q. Liu, S. Lu, G. Chen, S. Gao, S. Chen and X. Sun, *Sustainable Energy Fuels*, 2020, **4**, 3884–3887.
- 10 Y. Wang, T. Wang, R. Zhang, Q. Liu, Y. Luo, G. Cui, S. Lu, J. Wang, Y. Ma and X. Sun, *Inorg. Chem.*, 2020, **59**, 9491–9495.
- 11 X. Ji, B. Liu, X. Ren, X. Shi, A. M. Asiri and X. Sun, *ACS Sustainable Chem. Eng.*, 2018, **6**, 4499–4503.
- 12 G. Chen, T. Wang, J. Zhang, P. Liu, H. Sun, X. Zhuang, M. Chen and X. Feng, *Adv. Mater.*, 2018, **30**, 1706279.
- 13 G.-F. Chen, T. Y. Ma, Z.-Q. Liu, N. Li, Y.-Z. Su, K. Davey and S.-Z. Qiao, *Adv. Funct. Mater.*, 2016, **26**, 3314–3323.
- 14 P. Chen, T. Zhou, M. Zhang, Y. Tong, C. Zhong, N. Zhang, L. Zhang, C. Wu and Y. Xie, *Adv. Mater.*, 2017, **29**, 1701584.
- 15 J. Duan, S. Chen and C. Zhao, *Nat. Commun.*, 2017, **8**, 15341.
- 16 W. Lu, T. Liu, L. Xie, C. Tang, D. Liu, S. Hao, F. Qu, G. Du, Y. Ma, A. M. Asiri and X. Sun, *Small*, 2017, **13**, 1700805.
- 17 L. Xie, F. Qu, Z. Liu, X. Ren, S. Hao, R. Ge, G. Du, A. M. Asiri, X. Sun and L. Chen, *J. Mater. Chem. A*, 2017, **5**, 7806–7810.



- 18 R. Zhang, C. Tang, R. Kong, G. Du, A. M. Asiri, L. Chen and X. Sun, *Nanoscale*, 2017, **9**, 4793–4800.
- 19 T. Liu, D. Liu, F. Qu, D. Wang, L. Zhang, R. Ge, S. Hao, Y. Ma, G. Du, A. M. Asiri, L. Chen and X. Sun, *Adv. Energy Mater.*, 2017, **7**, 1700020.
- 20 D. Zhou, L. He, R. Zhang, S. Hao, X. Hou, Z. Liu, G. Du, A. M. Asiri, C. Zheng and X. Sun, *Chem. – Eur. J.*, 2017, **23**, 15601–15606.
- 21 C. Tang, R. Zhang, W. Lu, Z. Wang, D. Liu, S. Hao, G. Du, A. M. Asiri and X. Sun, *Angew. Chem., Int. Ed.*, 2017, **56**, 842–846.
- 22 L. Xie, R. Zhang, L. Cui, D. Liu, S. Hao, Y. Ma, G. Du, A. M. Asiri and X. Sun, *Angew. Chem., Int. Ed.*, 2017, **56**, 1064–1068.
- 23 C. Tang, R. Zhang, W. Lu, L. He, X. Jiang, A. M. Asiri and X. Sun, *Adv. Mater.*, 2017, **29**, 1602441.
- 24 X. Du, W. Lian and X. Zhang, *Int. J. Hydrogen Energy*, 2018, **43**, 20627–20635.
- 25 X. Du, Q. Shao and X. Zhang, *Int. J. Hydrogen Energy*, 2019, **44**, 2883–2888.
- 26 X. Du, H. Su and X. Zhang, *Int. J. Hydrogen Energy*, 2019, **44**, 21637–21650.
- 27 T. Tian, H. Gao, X. Zhou, L. Zheng, J. Wu, K. Li and Y. Ding, *ACS Energy Lett.*, 2018, **3**, 2150–2158.
- 28 T. Tian, M. Zheng, J. Lin, X. Meng and Y. Ding, *Chem. Commun.*, 2019, **55**, 1044–1047.
- 29 S. Li, J. Liu, S. Duan, T. Wang and Q. Li, *Chin. J. Catal.*, 2020, **41**, 847–852.
- 30 X.-B. Han, D.-X. Wang, E. Gracia-Espino, Y.-H. Luo, Y.-Z. Tan, D.-F. Lu, Y.-G. Li, T. Wågberg, E.-B. Wang and L.-S. Zheng, *Chin. J. Catal.*, 2020, **41**, 853–857.
- 31 X. Ren, D. Wu, R. Ge, X. Sun, H. Ma, T. Yan, Y. Zhang, B. Du, Q. Wei and L. Chen, *Nano Res.*, 2018, **11**, 2024–2033.
- 32 S. Tang, X. Li, M. Courté, J. Peng and D. Fichou, *Inorg. Chem. Front.*, 2020, **7**, 2241–2247.
- 33 S. Kandula, K. R. Shrestha, G. Rajeshkhanna, N. H. Kim and J. H. Lee, *ACS Appl. Mater. Interfaces*, 2019, **11**, 11555–11567.
- 34 G. Zhou, M. Li, Y. Li, H. Dong, D. Sun, X. Liu, L. Xu, Z. Tian and Y. Tang, *Adv. Funct. Mater.*, 2019, **30**, 1905252.
- 35 J. Zhu, M. Sun, S. Liu, X. Liu, K. Hu and L. Wang, *J. Mater. Chem. A*, 2019, **7**, 26975–26983.
- 36 C. Xia, Q. Jiang, C. Zhao, M. N. Hedhili and H. N. Alshareef, *Adv. Mater.*, 2016, **28**, 77–85.
- 37 X. Xu, F. Song and X. Hu, *Nat. Commun.*, 2016, **7**, 12324.
- 38 F. Hu, S. Zhu, S. Chen, Y. Li, L. Ma, T. Wu, Y. Zhang, C. Wang, C. Liu, X. Yang, L. Song, X. Yang and Y. Xiong, *Adv. Mater.*, 2017, **29**, 1606570.
- 39 X.-F. Lu, L.-F. Gu, J.-W. Wang, J.-X. Wu, P.-Q. Liao and G.-R. Li, *Adv. Mater.*, 2017, **29**, 1604437.
- 40 Y. Zhang, Y. Qiu, X. Ji, T. Ma, Z. Ma and P. A. Hu, *ChemSusChem*, 2019, **12**, 3792–3800.
- 41 H. Xu, J. Wei, K. Zhang, M. Zhang, C. Liu, J. Guo and Y. Du, *J. Mater. Chem. A*, 2018, **6**, 22697–22704.
- 42 K. Chi, X. Tian, Q. Wang, Z. Zhang, X. Zhang, Y. Zhang, F. Jing, Q. Lv, W. Yao, F. Xiao and S. Wang, *J. Catal.*, 2020, **381**, 44–52.
- 43 C. Xu, Q. Li, J. Shen, Z. Yuan, J. Ning, Y. Zhong, Z. Zhang and Y. Hu, *Nanoscale*, 2019, **11**, 10738–10745.
- 44 L. An, Y. Li, M. Luo, J. Yin, Y.-Q. Zhao, C. Xu, F. Cheng, Y. Yang, P. Xi and S. Guo, *Adv. Funct. Mater.*, 2017, **27**, 1703779.
- 45 J. Yin, Y. Li, F. Lv, M. Lu, K. Sun, W. Wang, L. Wang, F. Cheng, Y. Li, P. Xi and S. Guo, *Adv. Mater.*, 2017, **29**, 1704681.

## 文献收录检索证明

委托人	王海宾	单位	中北大学
<p>委托内容：</p> <p>检索委托人发表的文献“Experimental Investigation into the Damage Effect of Methane Explosion Shock Wave on Animals in Enclosed Pipeline”被 EI Compendex 数据库收录情况。</p>			
数据库名称	EI Compendex		
检索结果	<p>经数据库检索：</p> <p>委托检索的该篇文献被 EI 数据库收录。</p> <p>检索结果见检索页</p> <p>特此证明！</p>		
检索机构	<p>中北大学图书馆查新中心</p> 		
检索日期	2018.12.17	检索人	 ( 签字 )

## 1. Experimental Investigation Into the Damage Effect of Methane Explosion Shock Wave on Animals in Enclosed Pipeline

**Accession number:** 20184205960011

**Authors:** Wang, Hai-Bin (1); Zhao, Ying-Hu (2); Gao, Li (1); Tan, Ying-Xin (2); Wang, Lin-Bian (1); Yang, Liu (1)

**Author affiliation:** (1) School of Chemical Engineering and Technology, North University of China, Taiyuan; Shanxi; 030051, China; (2) School of Environment and Safety Engineering, North University of China, Taiyuan; Shanxi; 030051, China

**Corresponding author:** Tan, Ying-Xin(13934240901@163.com)

**Source title:** Binggong Xuebao/Acta Armamentarii

**Abbreviated source title:** Binggong Xuebao

**Volume:** 39

**Issue:** 8

**Issue date:** August 1, 2018

**Publication year:** 2018

**Pages:** 1639-1647

**Language:** Chinese

**ISSN:** 10001093

**CODEN:** BIXUD9

**Document type:** Journal article (JA)

**Publisher:** China Ordnance Society

**Abstract:** The pathological features and specific causes of lung, liver and spleen injury of rats induced by methane explosion in a pipeline are analyzed to provide evidences for the clinical treatment of injury caused by gas explosion. The damage effects of shock wave on the rats in different positions in the pipeline are observed by using the model of methane-air premixed gas explosion shock wave impacting on rats. The damage effect of shock wave on lung, liver and spleen and its mechanism are studied from the histopathology. The results show that the severity of injury of rat in the front end of pipeline is more serious than that in the rear end after the explosion of methane. However, the injury of its lung tissue at the rear end of pipeline is damaged by shock wave more significantly than that of rats in the front end. The alveolar collapse is obvious, and the connection between type lung cells and type lung cells is broken and disappeared. One of 5 rats died at the front end of pipeline, and 5 rats all died in the rear end of pipeline. The damage of liver tissue is mainly vacuolar degeneration of liver cells, blood sinus congestion, and significant hemorrhage. Some varying degrees of congestion, bleeding, inflammatory cell infiltration, and necrosis and abscission of bile duct epithelial cells appear in portal area. It is found that the neutrophils of survival animals were infiltrated. The injuries of lung, liver and spleen can be observed in methane explosion model. The lung injury is obvious and fatal. Microstructure and ultra-structure of lung indicate that lung is the most sensitive organ, which is the primary target organ impacted by shock wave. © 2018, Editorial Board of Acta Armamentarii. All right reserved.

**Number of references:** 18

**Main heading:** Shock waves

**Controlled terms:** Biological organs - Cells - Cytology - Explosions - Methane - Pipelines - Rating - Rats - Tissue

**Uncontrolled terms:** Clinical treatments - Epithelial cells - Experimental investigations - Inflammatory cells - Lung - Methane explosions - Severity of injuries - Ultra structure

**Classification code:** 461.2 Biological Materials and Tissue Engineering - 619.1 Pipe, Piping and Pipelines - 804.1 Organic Compounds - 931 Classical Physics; Quantum Theory; Relativity

**DOI:** 10.3969/j.issn.1000-1093.2018.08.022

**Compendex references:** YES

**Database:** Compendex

Compilation and indexing terms, Copyright 2018 Elsevier Inc.

**Data Provider:** Engineering Village



# 甲烷爆炸冲击波作用下密闭管道内 动物损伤效应试验研究

王海宾<sup>1</sup>, 赵英虎<sup>2</sup>, 高莉<sup>1</sup>, 谭迎新<sup>2</sup>, 王林变<sup>1</sup>, 杨柳<sup>1</sup>

(1. 中北大学 化学工程与技术学院, 山西 太原 030051; 2. 中北大学 环境与安全工程学院, 山西 太原 030051)

**摘要:** 通过观察管道内甲烷爆炸对大鼠的肺等组织损伤病理特征, 分析损伤原因, 为瓦斯爆炸伤的临床救治提供依据。采用甲烷-空气预混气体爆炸冲击波对密闭管道内大鼠的作用模型, 观察冲击波对管道内不同位置大鼠的损伤程度, 并从病理组织学角度分析冲击波作用下肺、肝、脾组织损伤效应及机理。结果表明: 密闭管道内, 甲烷爆炸后置于管道前端的大鼠灼伤程度比置于后端的大鼠严重, 但后端大鼠的肺组织受到的冲击波损伤比前端大鼠更为显著, 肺泡发生明显塌陷, I型肺细胞和II型肺细胞连接断裂并消失, 管道前端的5只大鼠死亡1只, 管道后端的5只大鼠全部死亡; 肝组织的损伤主要是肝细胞空泡样变性、血窦淤血、出血明显, 汇管区有不同程度的淤血、出血、炎性细胞浸润及胆管上皮细胞坏死脱落; 甲烷爆炸对大鼠的肺、肝、脾均造成损伤, 但肺部损伤明显且形成致命损伤, 肺显微结构和超微结构显示肺部对爆冲击波压力最为敏感, 是冲击波作用的主要靶器官。

**关键词:** 甲烷; 爆炸; 冲击波; 大鼠; 肺

中图分类号: O384; S857.8<sup>+</sup>6

文献标志码: A

文章编号: 1000-1093(2018)08-1639-09

DOI: 10.3969/j.issn.1000-1093.2018.08.022

## Experimental Investigation into the Damage Effect of Methane Explosion Shock Wave on Animals in Enclosed Pipeline

WANG Hai-bin<sup>1</sup>, ZHAO Ying-hu<sup>2</sup>, GAO Li<sup>1</sup>, TAN Ying-xin<sup>2</sup>, WANG Lin-bian<sup>1</sup>, YANG Liu<sup>1</sup>

(1. School of Chemical Engineering and Technology, North University of China, Taiyuan 030051, Shanxi, China;

2. School of Environment and Safety Engineering, North University of China, Taiyuan 030051, Shanxi, China)

**Abstract:** The pathological features and specific causes of lung, liver and spleen injury of rats induced by methane explosion in a pipeline are analyzed to provide evidences for the clinical treatment of injury caused by gas explosion. The damage effects of shock wave on the rats in different positions in the pipeline are observed by using the model of methane-air premixed gas explosion shock wave impacting on rats. The damage effect of shock wave on lung, liver and spleen and its mechanism are studied from the histopathology. The results show that the severity of injury of rat in the front end of pipeline is more serious than that in the rear end after the explosion of methane. However, the injury of its lung tissue at the rear end of pipeline is damaged by shock wave more significantly than that of rats in the front end. The alveolar collapse is obvious, and the connection between type I lung cells and type II lung cells is broken.

收稿日期: 2017-12-12

基金项目: 山西省科技攻关项目(20140311008-7); 纳米功能复合材料山西省重点实验室开放基金项目(NFCM201603); 山西省自然科学基金青年基金项目(20170402SJJ)

作者简介: 王海宾(1975—), 男, 副教授, 博士。E-mail: whaibin@nuc.edu.cn

通信作者: 谭迎新(1964—), 女, 教授, 博士生导师。E-mail: 13934240901@163.com

ken and disappeared. One of 5 rats died at the front end of pipeline, and 5 rats all died in the rear end of pipeline. The damage of liver tissue is mainly vacuolar degeneration of liver cells, blood sinus congestion, and significant hemorrhage. Some varying degrees of congestion, bleeding, inflammatory cell infiltration, and necrosis and abscission of bile duct epithelial cells appear in portal area. It is found that the neutrophils of survival animals were infiltrated. The injuries of lung, liver and spleen can be observed in methane explosion model. The lung injury is obvious and fatal. Microstructure and ultra-structure of lung indicate that lung is the most sensitive organ, which is the primary target organ impacted by shock wave.

**Key words:** methane; explosion; shock wave; rat; lung

## 0 引言

随着科学技术的不断进步,武器装备及战略战术发生了重大转变。爆炸性大规模杀伤性武器在现代高科技局部战争中的使用越来越广泛、威力越来越大<sup>[1]</sup>。此外,矿山瓦斯、企业粉尘、施工炸药及沼气、煤气等意外爆炸事故时有发生,加之局部暴力冲突及恐怖活动的日益猖獗,使爆炸伤的发生率明显升高<sup>[2]</sup>。爆炸性武器的主要杀伤因素是破片和冲击波。爆炸性武器破片伤的发生率为 53%~81%,冲击伤的发生率为 30.0%~50.4%<sup>[3]</sup>。各类爆炸产生的剧烈震动对动物是一种强烈刺激,可能会导致应激反应。由于脏器的功能活动受神经内分泌调节,当其发生异常改变后,可能会导致脏器发生病理改变。在日常生活、军事作业和战场作战中,爆炸产生的损伤是造成人民生命财产损失和战斗力减员的重要因素。因此,加强爆炸致伤的生物效应研究具有重要的军事意义和实际应用价值<sup>[4]</sup>。

爆炸物周围的空气介质接受膨胀所传递的能量后形成压缩波,多个压缩波重叠后形成了冲击波。爆炸冲击波压力变化的时间极短,但是变化的幅度和速度极高,破坏力非常大,能造成人体多系统器官损伤甚至伤亡。爆炸冲击波对人体的损伤主要集中在含有空气的生物器官,如耳膜、肺及肠胃<sup>[5]</sup>。Argyros<sup>[6]</sup>指出,冲击波对肺的损伤是使人致命的关键因素。冲击波作用于人体胸部时,诱发生物组织产生应力波并在肺组织中传播,从而导致肺泡破裂、撕裂、内爆裂<sup>[7-8]</sup>。

由于煤炭事故频发,瓦斯爆炸给人民生命财产造成巨大损失,科学家们更多关注瓦斯爆炸火焰的传播规律、引起煤尘二次爆炸的机理、障碍物对爆炸特性的影响等,但对于密闭空间内甲烷爆炸对动物损伤的研究较少。本文选择甲烷气体为研究对象,以大鼠作为模型动物,在模拟管道内进行 10% 甲烷-空气预混气体爆炸冲击波对不同位置的动物损

伤生物学效应与损伤机理进行研究。

## 1 材料和方法

### 1.1 试验材料

试验所用大鼠购于山西医科大学实验动物中心(批号 SCXK2009-0001)的 6 月龄大鼠,体质量( $200 \pm 20$ ) g,10 只,雌雄各半。甲烷气体购于山西海同利气体有限公司,纯度为 99.99%。

### 1.2 爆炸试验设备测试装置

采用自行设计的管道式爆炸装置,该装置由爆炸管、配气系统、压力测试系统、火焰速度测试系统、高压点火系统组成。用于本试验的管道总长 3.1 m,由 3 段无缝钢管组成,长度分别为 0.7 m、1.2 m、1.2 m,管道内径为 0.139 m、壁厚为 0.01 m,中间由法兰连接,靠螺栓紧固,另有石棉垫片和胶皮垫片密封,末端由盲法兰封闭。在距左端盲法兰 0.25 m 处装有一对点火电极。管道上依次安装了 4 个压电式压力传感器,分别称为测点 1、测点 2、测点 3 和测点 4。在管道第 1 节上装有真空压力表,左边的盲法兰上开有配气接口。爆炸管的每节管道上均设有观察孔,其中观察孔 2~3 上可以安装火焰探测器,通过火焰经过 2 个火焰探测器测量的时间来测量火焰传播的平均速度,观察孔 2 和观察孔 3 之间的距离为 2.25 m。安全阀安装在爆炸管道右端,当压力超过 2 MPa 时安全阀自动泄压。管道式爆炸装置结构示意图如图 1 所示。

### 1.3 动物分组及布放

采用自行设计的双层笼对大鼠进行固定。将装有大鼠的笼子分别编号,1 号笼子放于距离点火源 115 cm 处(前端),2 号笼子放于距离点火源 226 cm 处(后端)。管道上依次安装 2 个压电式压力传感器,分别位于测点 2 和测点 4,分别编号为 2 号传感器和 4 号传感器。采用分压配气法进行配气,气体混合均匀后进行点火起爆,压力传感器可测得瞬间爆炸压力。爆炸并泄压后对大鼠进行死亡、灼伤程

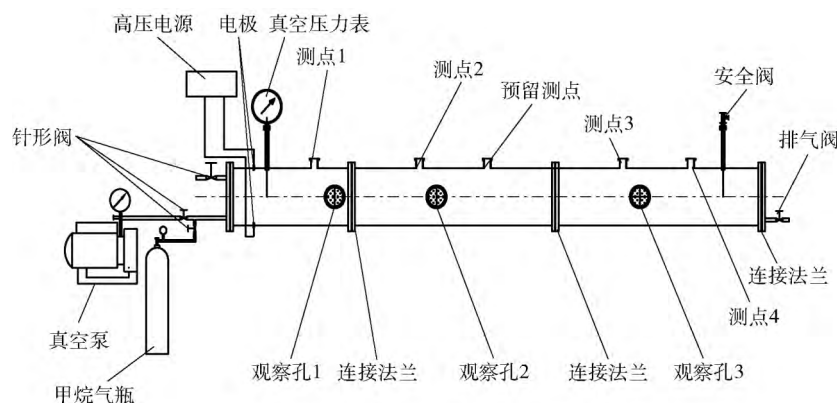


图1 管道式爆炸装置示意图

Fig. 1 Schematic diagram of pipelined explosive device

度等损伤观察。

#### 1.4 甲烷爆炸试验方法

利用甲烷-空气预混气体的爆炸过程研究在密闭管道内甲烷爆炸对动物的灼伤程度、冲击波对管道内不同位置大鼠的肺、肝、脾等组织损伤变化。根据前期试验结果<sup>[8]</sup>，在该装置中甲烷浓度为10%时反应最剧烈，产生的爆炸威力最大，因此选择的甲烷浓度为10%。检查管道气密性后，将大鼠置于笼中并置于管道内，采用分压法<sup>[9]</sup>配制所需浓度的可燃气体，给点火电极上加高压使其产生电火花，引燃产生爆炸冲击波，由数据采集系统记录试验结果。具体步骤为：1) 气密性检测，在管道内通过空压机充入一定压力的空气，保压10 min，以压力不下降为合格；2) 安装火焰测速仪（根据试验需要进行安装）；3) 安装圆环形障碍物（根据试验需要进行安装）；4) 将大鼠固定笼放入设计的位置；5) 开启真空泵15 s，将管道内抽成真空（0.02 MPa）；6) 打开甲烷钢瓶阀门，通过配气管向管道内充入甲烷，当甲烷气体的分压达到试验所要求气压时停止进气（10 s）；7) 打开阀门向管道中充入空气，当管内混合气体的压力达到1个标准大气压时，停止进气（15 s）；8) 打开高压点火器电源并充电到指定电压，启动数据采集仪与火焰测速仪等待触发状态，点火；9) 记录数据。

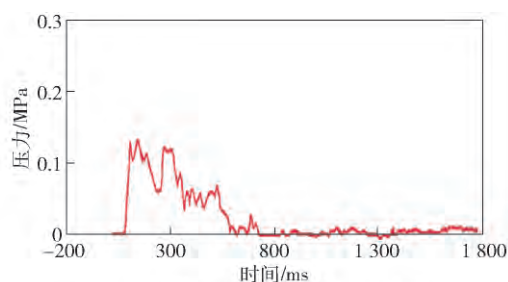
#### 1.5 观察指标

爆炸泄压后取出大鼠进行损伤程度观察。对心跳、呼吸已经停止的大鼠判为即刻死亡者，并立即进行解剖观察；如果大鼠存活，经颈动脉放血处死后再进行解剖，观察肺、肝、脾组织的损伤情况。组织取材后，分别用40 mg/L多聚甲醛和戊二醛固定，用常规石蜡包埋切片、HE染色，并用光镜和电镜观察组织形态学变化。

## 2 试验结果与分析

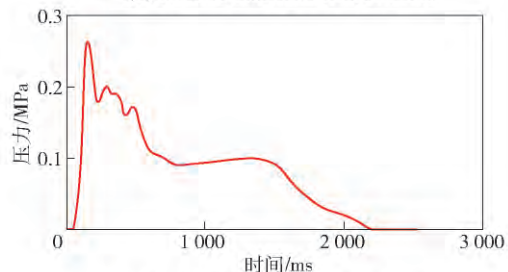
### 2.1 管道内甲烷爆炸后物理参数检测及动物损伤情况观察

在甲烷浓度为10%的管道内，引爆后2号传感器和4号传感器分别测得压力为0.149 MPa和0.264 MPa，爆炸压力曲线如图2所示。泄压后，对置于管道前端与后端的大鼠进行生命体征、灼伤程度观察记录。随后立即对大鼠进行解剖并对肺外部特征如颜色变化、出血情况进行观察，观察结果如表1所示。



(a) 2号传感器测得压力-时间曲线

(a) Pressure-time curve from Sensor 2



(b) 4号传感器测得压力-时间曲线

(b) Pressure-time curve from Sensor 4

图2 传感器测得压力-时间曲线

Fig. 2 Pressure-time curves from sensors

置于管道前端的5只大鼠死亡1只，管道后端的大鼠灼伤程



表 1 不同部位爆炸压力值与大鼠损伤情况

Tab. 1 Burns and pulmonary hemorrhage of rats			
指标	正常大鼠	管道前端的大鼠	管道后端的大鼠
爆炸压力/ MPa	0	0.149	0.264
生命状态	正常	濒临死亡	死亡
外部形态	正常	皮毛灼伤明显,约 70%的面积过火灼 伤 部分区域烧焦	皮毛灼烧较明显, 约 50% 的面积有 过火、灼伤
肺部表现	淡粉色, 有光泽	红色,无光泽,充血 明显,可见点片状 出血	无光泽,两侧肺呈 疙瘩块状出血

度比置于后端的大鼠严重(见图 3(a)和图 3(b)),但解剖发现置于后端大鼠的肺出血程度却远高于前端大鼠。置于前端大鼠的肺充血,呈现片状出血现象(见图 3(c))。置于后端的大鼠两侧肺呈现较均匀的块状出血(见图 3(d))。

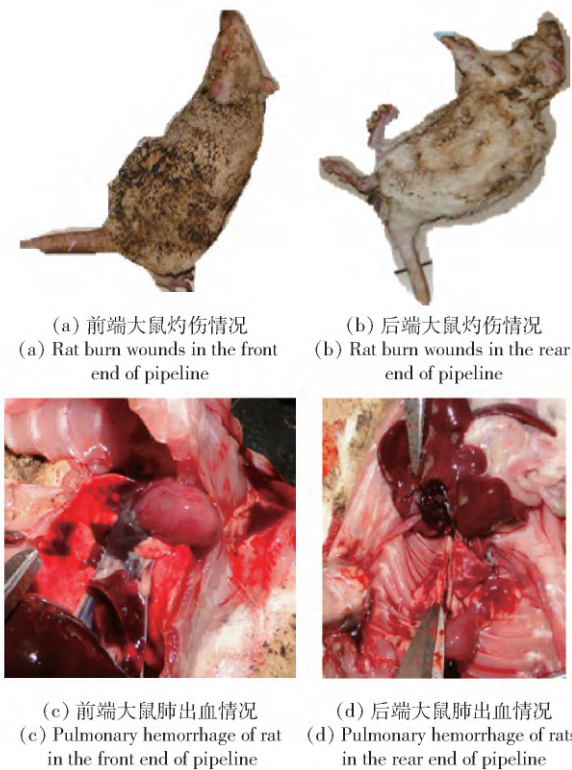


图 3 大鼠灼伤及肺出血情况

Fig. 3 Rat burns and pulmonary hemorrhage

2.2 密闭管道内甲烷爆炸后大鼠肺、肝、脾组织病理学改变

2.2.1 密闭管道内甲烷爆炸后大鼠肺组织病理学改变

图 4 所示为甲烷爆炸对大鼠肺的显微结构改变。

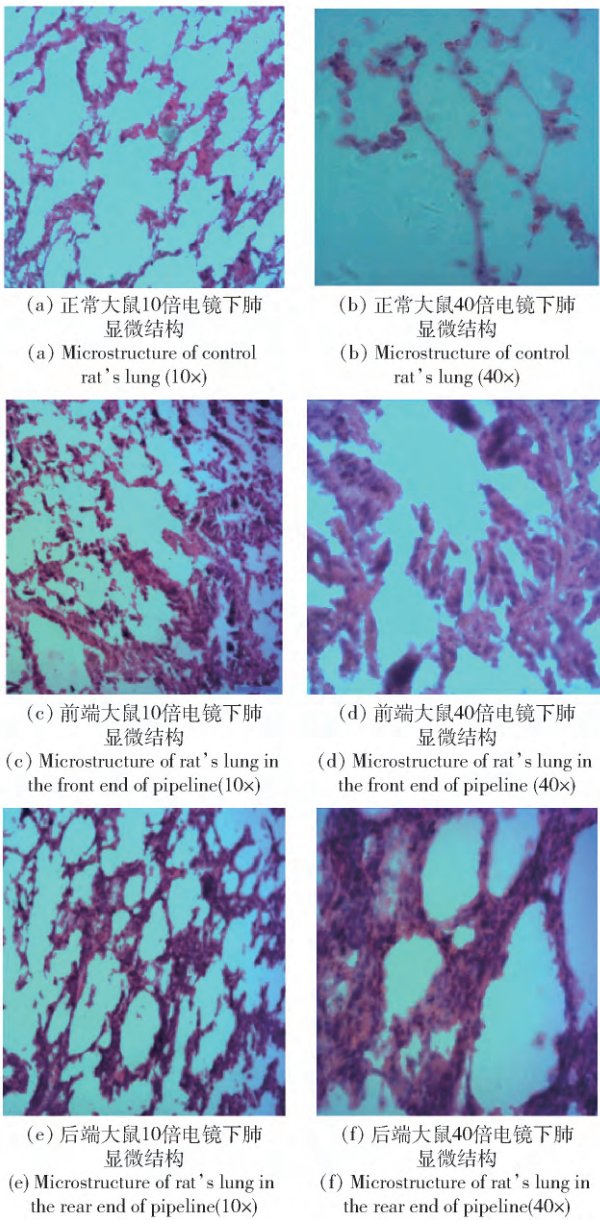


图 4 甲烷爆炸对大鼠肺显微结构改变

Fig. 4 Changes of lung microstructures of rats exposed to methane explosion

由图 4(a)可见,正常大鼠的肺显微结构显示肺泡排列整齐,肺泡隔(相邻肺泡间含有丰富毛细血管网和弹性纤维的薄层结缔组织)基本均匀。呼吸性支气管、终末性细支气管完整。

由图 4(b)可以看到,完整且彼此相连的肺泡以及肺泡隔上的少量红细胞,肺细胞核规则且位于细胞中央。

由图 4(c)可以看到:置于前端的大鼠肺组织脱落物增多,多数肺泡塌陷,呈现不规则状态;肺泡隔增厚、堆积,红细胞较多,肺泡发生空泡化,终末性细支气管破裂,视眼内有少量黑色颗粒。

由图 4(d) 可以看到, 终末性呼吸性器官破裂, 单层柱状上皮散落, 多数肺泡破裂、堆积。

由图 4(e) 可见: 置于后端的大鼠肺组织中明显看到一个大的空腔而且几乎所有肺泡挤压在一起, 很少能看到规则的肺泡且出血明显; 红细胞呈弥散性遍布, 并发生堆积挤压, 基本无正常肺泡, 绝大多数肺泡塌陷, 肺泡隔增厚, 脱落物增多, 视眼内有大量黑色颗粒。

由图 4(f) 可见, 肺泡隔重叠、挤压, 形成较厚的堆积层, 细胞核边缘化, 出现肺水肿特征。

### 2.2.2 密闭管道内甲烷爆炸后大鼠肝组织病理学改变

图 5 所示为甲烷爆炸对大鼠肝显微结构改变。

由图 5(a) 可以看出: 正常大鼠的肝显微结构由排列不整齐的单行肝细胞构成, 形成迷路样条索状的肝板; 中央静脉常位于肝小叶中央, 在肝板之间的网状管道——肝血窦, 使血液从肝小叶周边经血窦汇入中央静脉。

由图 5(b) 可以看出, 在高倍电镜下可以清楚地看到一个核或两个核的肝细胞, 肝板连续完整, 肝血窦腔基本均匀<sup>[10]</sup>。

由图 5(c) 可以看出, 置于前端大鼠在受到冲击波作用后, 肝细胞出血明显, 中央静脉变形, 肝板断裂、残留, 呈无规则状。

由图 5(d) 可以看出, 肝窦腔增大, 肝板变短, 肝细胞核边缘化, 有的肝细胞出现变形。

由图 5(e) 可以看出, 置于后端的大鼠在受到冲击波作用后, 肝细胞中央静脉变形, 出血程度高于前端大鼠, 肝板断裂。

由图 5(f) 可以看出, 40 倍电镜下可看到肝细胞核变小, 部分出现无核化。

综上所述可知, 前后两端大鼠的肝细胞均受到不同程度的冲击, 后端大鼠的肝损伤略为明显, 部分肝细胞受损、死亡, 肝窦腔增大, 肝板断裂导致部分肝功能受损。这一结论与李泽信等<sup>[11]</sup>在研究肝脏的火器伤所观察到的肝细胞形态变化基本一致。

### 2.2.3 密闭管道内甲烷爆炸后大鼠脾组织病理学改变

图 6 所示为甲烷爆炸对大鼠脾显微结构改变。

脾是免疫应答的重要场所, 可构成机体免疫的第 3 道防线。脾由被膜、小梁、白髓、红髓、边缘区 5 部分组成, 具有滤血、储血和造血功能<sup>[12]</sup>。在脾的新鲜切片上呈散布的灰白色小点状, 故名“白髓”。红髓含有大量的红细胞, 因此显红色。

由图 6(a) 可见: 染色后呈现着色较深的致密蓝色区域为白髓, 该区域含有大量 T 细胞、少量巨噬

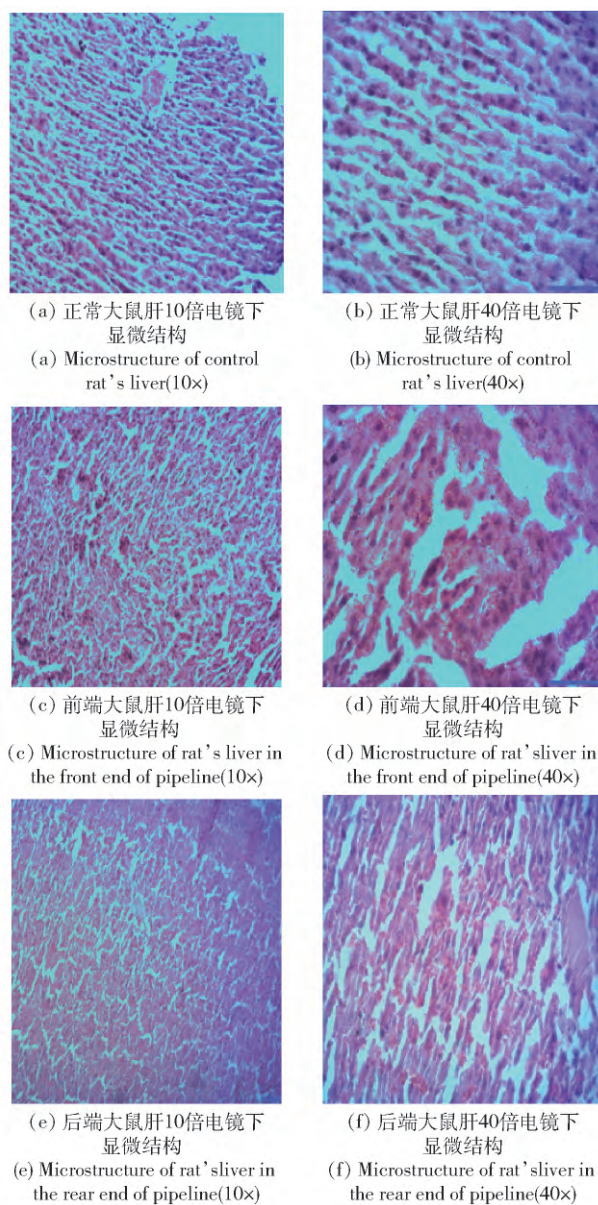


图 5 甲烷爆炸对大鼠肝显微结构改变

Fig. 5 Changes of liver microstructures of rats exposed to methane explosion

细胞; 着色较浅、细胞排列稀疏的区域为红髓, 该区域含有 T 细胞、B 细胞、浆细胞、巨噬细胞和其他细胞。

由图 6(b) 可见, 红髓和白髓的交界处细胞排列较白髓稀疏, 较红髓密集, 在光学显微镜下呈现蓝色和红色的区域为边缘区, 该区域是脾内免疫细胞捕获、识别、处理抗原和诱发免疫应答的重要部分。红髓区脾索排列整齐, 细胞核居中并呈椭圆形, 脾窦腔基本规则均匀<sup>[10]</sup>。

由图 6(c) 可见, 置于前端的大鼠脾在受到冲击波作用后, 白髓着色变浅、区域缩小, 红髓变得更加



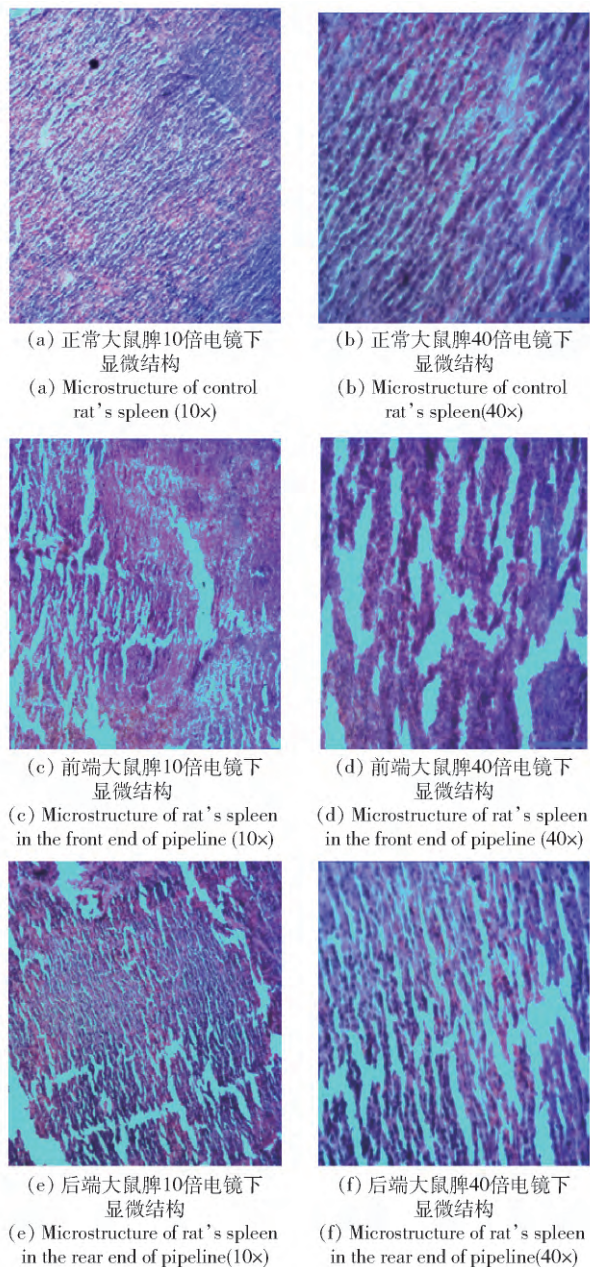


图6 甲烷爆炸对大鼠脾显微结构改变

Fig. 6 Changes of spleen microstructures of rats exposed to methane explosion

稀疏、脾索断裂、残留、脾窦腔增大并伴有出血。

由图 6 (d) 可见,脾索无规则、堆积挤压,脾窦腔有的增大、有的缩小,细胞核边缘化。

后端大鼠脾的白髓和红髓界限不清,出血明显(见图 6 (e));基本脾索挤压、部分断裂,脾窦出血(见图 6 (f))。

综上所述可见,置于前后端大鼠脾的显微结构损伤类似,没有显著差异。这是因为脾的主要功能是进行免疫应答,在受到冲击波作用后由于肺部和肝部同样也受到冲击波作用而引起炎症反应,但是

瞬间的冲击已经使后端大鼠死亡,免疫应答基本不会做出多余反应<sup>[13]</sup>。前端大鼠虽然没有当场死亡,但是肺部损伤也使其奄奄一息,同时在爆炸试验结束后就对其处死并立即进行了解剖,因此免疫反应也基本没有。

脾所受到的冲击作用更多地表现为自身所受到的损伤,且前后端大鼠的脾损伤程度基本相当。当然在这个过程中大鼠的脾显微结构明显发生了脾索断裂、残留以及脾窦腔、脾细胞核边缘化等改变引起的脾功能性损伤。

### 2.3 大鼠肺超微结构的改变与分析

正常大鼠的肺超微结构显示,肺泡由 I 型和 II 型两种肺泡细胞组成,二者紧密相连。其中, I 型肺泡覆盖了肺泡表面的绝大部分,细胞大而扁薄,表面光滑,含核部分略厚,其余部分薄,胞核扁圆,胞质内细胞器甚少,吞饮小泡较多,参与构成血-气屏障。II 型肺泡细胞数量较多,胞体较小,呈立方形或圆形,嵌于 I 型肺泡细胞之间。胞内线粒体完整且嵴(线粒体内膜向线粒体基质折褶形成的一种结构)清晰。胞核呈圆形,胞质淡染,呈泡沫状。胞质内有许多呈同心圆或平行排列的板层结构,称嗜锇性板层小体,即分泌颗粒。小体大小不一,直径为  $0.1 \sim 1.0 \mu\text{m}$ ,其电子密度高,主要含二棕榈酰卵磷脂。细胞以胞吐方式将其分泌到肺泡表面并铺一层薄膜,称表面活性物质。肺泡隔是由相邻肺泡间丰富毛细血管网和弹性纤维构成的薄层结缔组织。肺巨噬细胞由单核细胞分化而来,胞体较大,形状不一,具有游走性和活跃的吞噬能力。

置于前端大鼠受冲击波作用后其肺 I 型细胞和 II 型细胞连接消失,多数挤压堆积。多数细胞内线粒体嵴消失甚至空洞化。一些 I 型细胞出现无核化,如图 7 (b) 所示;巨噬细胞空洞化,如图 7 (h) 所示。

置于后端大鼠肺受冲击波作用后其 I 型肺细胞和 II 型肺细胞连接全部断裂并消失。I 型肺细胞核拉伸变形,如图 7 (c) 所示。II 型肺细胞核碎裂,线粒体空洞,细胞间挤压更加紧密,肺泡腔基本消失,如图 7 (f) 所示。巨噬细胞出现空洞化,肺细胞多数已经坏死,丧失了细胞基本功能,如图 7 (i) 所示。

肺细胞的超微结构进一步证明,置于后端的大鼠肺部受到的冲击波作用相当严重,肺泡几乎完全塌陷,肺细胞损伤殆尽,肺的血-气交换功能完全丧失。同时在此次试验中还发现,不论是肺显微结构还是超微结构中,也不论是放置在前端还是后端,大

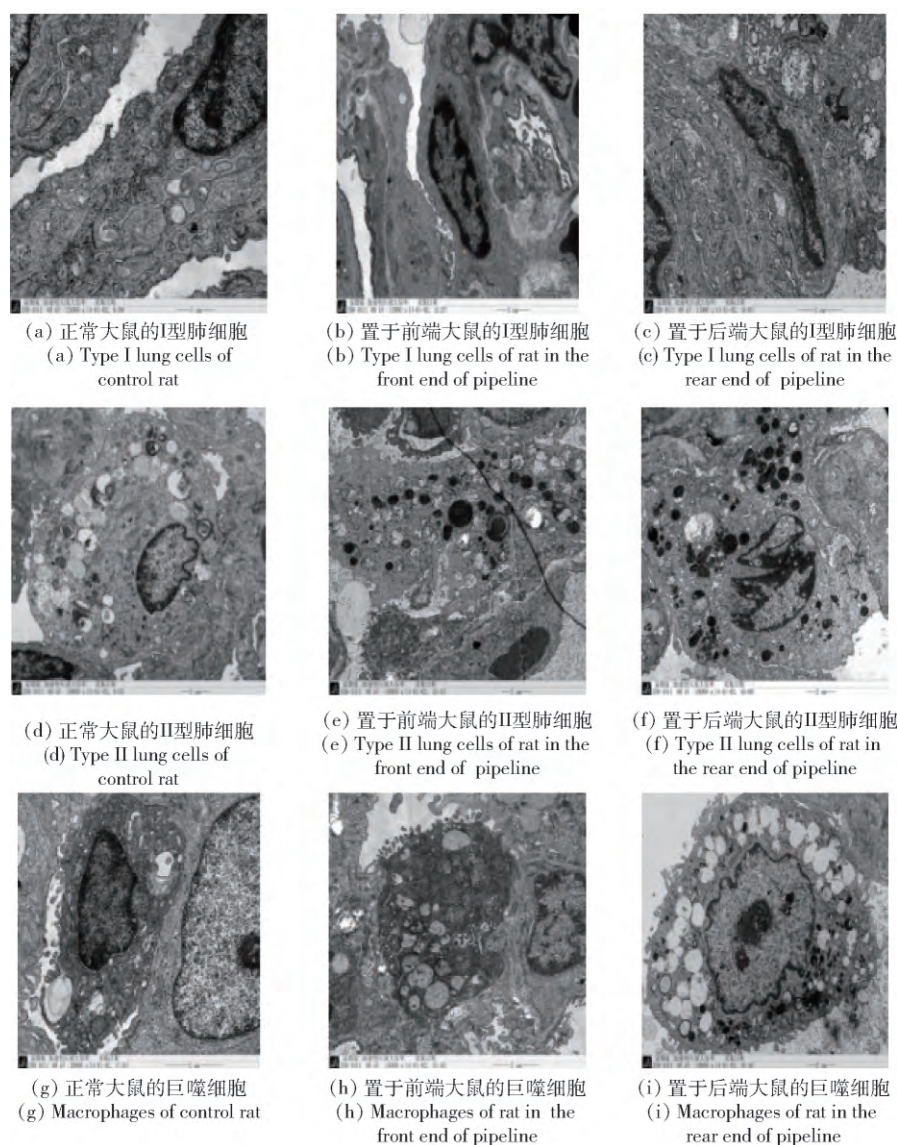


图 7 甲烷爆炸对大鼠肺超微观结构改变

Fig. 7 Changes of lung ultrastructures of rats exposed to methane explosion

鼠肺泡中均有黑色颗粒物质,如图 7( e)、图 7( f)、图 7( i) 所示。由此可见,多次试验的结果已经证明大鼠在死亡前曾呼吸了含有碳微颗粒的空气。

### 3 冲击波对动物组织的损伤分析

本文试验结果显示,置于管道前端的大鼠灼伤程度比置于后端的大鼠严重。分析认为在甲烷-空气预混气体管道内,置于前端的点火源引爆后,前端的甲烷开始迅速燃烧并对大鼠造成灼伤,随着时间的推进,燃烧速度呈现快速递增,温度升高,压力快速上升。置于后端的大鼠所承受的压力增大,但火焰通过大鼠的燃烧时间较前端大鼠短暂。置于后端的大鼠生命状态是死亡,其肺出血程度远高于前端大鼠。分析认为后端大鼠受到的冲击波伤害大于前

端大鼠,肺泡损伤塌陷程度显著,肺泡隔的血-气屏障遭到破坏,基本丧失了气与血交换能力<sup>[14]</sup>。如果肺组织没有换气功能,也就没有了呼吸作用。这也是前端大鼠濒临死亡而没有断气、而置于后端的大鼠已经停止呼吸的一个重要原因。另外,文献[15-16]认为正向冲击波作用在封闭管道内后壁会反射,并沿其周围衍射。反射波面向源头反向行进,反射波冲击物体时,物体表面产生的压力远远大于波的峰值静态压力。文献[17]研究发现,理想气体在冲击波作用下碰到刚性墙壁发生反射时,向前移动的空气分子停止于墙上,其后继续移动分子仍然压迫波前停滞的分子,此时墙上物体的总压力是静态压力和动态压力的总和。因此,在本试验密闭管道环境中大鼠会接触多方向的反射波,在机体上产



生累加效应,导致冲击伤程度更重、死亡几率更高的是后端大鼠,而前端大鼠随着反射波的衰减所受到的损伤没有达到致死程度。在本试验中还发现,不论是前端大鼠还是后端大鼠,损伤的肺细胞中均出现黑色颗粒。可以推断,管道内甲烷燃烧爆炸后,火焰通过灼伤使前端大鼠的皮毛产生了碳颗粒,正向冲击波作用于后端大鼠的瞬间可能没有造成死亡,因此后端大鼠有机会继续呼吸带有碳颗粒的空气,从而在肺泡内留下了微小黑色颗粒。而反向冲击波造成后端大鼠死亡,前端大鼠呼吸了含有碳微粒的空气,并留在肺泡内。综上所述可以认为,在密闭环境中反射波的压力更大、更致命。

置于后端大鼠的肝损伤比前端大鼠严重,部分肝细胞受损、死亡,肝窦腔增大,肝板断裂导致大鼠部分肝功能受损,影响其生存状态和伤后恢复。因为肝不仅是动物体内最大的消化腺,可以分泌胆汁、促进脂肪的分解与吸收,而且也是一个极其重要的物质代谢器官,参与多种物质的合成、贮存、代谢和转化<sup>[10]</sup>。该试验中肝窦腔增大、肝板断裂导致的肝功能受损会影响正常的物质代谢,但不至于导致大鼠立即死亡。这一结论与李泽信等<sup>[11]</sup>在研究肝脏的火器伤中所得出的结论基本一致。

置于后端的大鼠脾损伤程度与前端大鼠相似,没有显著差异,脾的损伤程度不是导致后端大鼠死亡的根本原因。分析认为脾的主要功能是进行免疫应答,脾所受到的冲击作用更多地表现为自身所受到的损伤,且前后端大鼠的脾损伤程度基本相当。当然通过脾的显微结构可明显发现大鼠的脾索断裂、残留,脾窦腔、脾细胞核边缘化等改变引起脾功能性损伤,但不是致死的根本原因。唐献述等<sup>[18]</sup>通过近地表爆炸空气冲击波对动物的伤害效应试验研究,也证实了上述观点。

#### 4 结论

1) 在甲烷-空气预混气体管道内,引爆后前端的甲烷开始迅速燃烧并对大鼠造成灼伤,置于管道前端的大鼠灼伤程度比置于后端的大鼠严重,但后端大鼠的肺组织受到冲击波损伤的程度明显高于前端大鼠。

2) 管道前端的 5 只大鼠死亡 1 只,管道后端的 5 只大鼠全部死亡。爆炸对大鼠肺、肝、脾均造成损伤,但肺部损伤更明显。

3) 肺显微结构和超微结构显示,肺受冲击波作用后 I 型肺细胞和 II 型肺细胞连接全部断裂并消

失。I 型肺细胞核拉伸变形,II 型肺细胞核碎裂,线粒体空洞,肺泡腔基本消失。巨噬细胞空洞化,肺泡几乎完全塌陷,肺细胞损伤殆尽,肺的血与气交换功能完全丧失,导致死亡。

4) 肝和脾虽均有损伤但未形成致命损伤,肺部对爆冲击波压力最为敏感,是冲击波作用的主要靶器官。

#### 参考文献(References)

- [1] 秦俊华. 爆炸冲击波对人体创伤效应评估软件设计[D]. 南京: 南京理工大学, 2017.  
QIN Jun-hua. Software design of safety assessment of explosive shock wave on human[D]. Nanjing: Nanjing University of Science and Technology, 2017. (in Chinese)
- [2] 杨策, 蒋建新, 杜娟, 等. 2000 年至 2015 年国内 174 起爆炸事故冲击伤诊治分析[J]. 中华诊断学: 电子杂志, 2016, 4(1): 36-40.  
YANG Ce, JIANG Jian-xin, DU Juan, et al. Analysis of the current situation of diagnosis and therapy in Chinese severe explosion accidents over the past 15 years [J]. Chinese Journal of Diagnostics: Electronic Edition, 2016, 4(1): 36-40. (in Chinese)
- [3] Cernak I, Savic J, Ignjatovic D, et al. Blast injury from explosive munitions[J]. Journal of Trauma, 1999, 47(1): 96-103.
- [4] Sukubo N G, Tibalt E, Respizzi S, et al. Effect of shock waves on macrophages: a possible role in tissue regeneration and remodeling [J]. International Journal of Surgery, 2015, 24(Part B): 124-130.
- [5] D'Yachenko A I, Manyuhina O V. Modeling of weak blast wave propagation in the lung [J]. Journal of Biomechanics, 2006, 39(11): 2113-2122.
- [6] Argyros G J. Management of primary blast injury[J]. Toxicology, 1997, 121(1): 105-115.
- [7] Geer A D. Numerical modeling for the prediction of primary blast injury to the lung[D]. Ontario, Canada: University of Waterloo, 2006.
- [8] 尉存娟, 谭迎新, 郝永飞, 等. 密闭管道内障碍物对瓦斯爆炸压力的影响[J]. 煤炭科学技术, 2013, 41(7): 86-88.  
YU Cun-juan, TAN Ying-xin, HAO Yong-fei, et al. Influence on gas explosion pressure by obstacles in the close tube [J]. Coal Science and Technology, 2013, 41(7): 86-88. (in Chinese)
- [9] Baker W E, Cox P A, Westine J J, 等. 爆炸危险性及其评估[M]. 张国顺, 文以民, 刘定吉, 等, 译. 北京: 群众出版社, 1988.  
Baker W E, Cox P A, Westine J J, et al. Explosion hazards and evaluation[M]. ZHANG Guo-shun, WEN Yi-min, LIU Ding-ji, et al, translated. Beijing: Masses Publishing House, 1988. (in Chinese)
- [10] 沈霞芬. 家畜组织学与胚胎学[M]. 第 4 版. 北京: 中国农业出版社, 2011.  
SHEN Xia-fen. Histology and embryology of domestic animals

- [M]. 4th ed. Beijing: China Agriculture Press 2011. (in Chinese)
- [11] 李泽信,冯德元,张永久,等. 猪腹部火器伤肠管穿透后肝脏功能和形态的变化[J]. 中国现代普通外科进展, 2007, 10(1): 45-47.
- LI Ze-xin, FENG De-yuan, ZHANG Yong-jiu, et al. Changes of hepatic morphology and function following intestinal perforation due to abdominal firearm wound in pigs[J]. Chinese Journal of Current Advances in General Surgery, 2007, 10(1): 45-47. (in Chinese)
- [12] 尉存娟. 水平管道内甲烷-空气预混气体爆炸过程研究[D]. 太原: 中北大学, 2010.
- YU Cun-juan. Research of explosion process on premix gas of methane-air in horizontal pipeline[D]. Taiyuan: North University of China 2010. (in Chinese)
- [13] 张旭,黄怀,陈辉强,等. 高压氧治疗对脊髓损伤大鼠脾脏组织病理的影响[J]. 广州医学院学报, 2013, 41(3): 35-37, 44.
- ZHANG Xu, HUANG Huai, CHEN Hui-qiang, et al. Effects of hyperbaric oxygen therapy on splenocytes in rats with spinal cord injury[J]. Academic Journal of Guangzhou Medical College, 2013, 41(3): 35-37, 44. (in Chinese)
- [14] 李唯,贾克勇,李焕章,等. 8 Hz 和 16 Hz 次声波对大鼠肺组织及肺氧合功能的影响[J]. 第四军医大学学报, 2001, 22(16): 1485-1489.
- LI Wei, JIA Ke-yong, LI Huan-zhang, et al. Changes of oxygenation and lung damage after different decibel of 8 Hz and 16 Hz infrasound operated on rats[J]. Journal of the Fourth Military Medical University, 2001, 22(16): 1485-1489. (in Chinese)
- [15] 康建毅,王建民,喻永敏,等. 爆炸冲击波载荷下的人体胸部有限元模型数值模拟研究[J]. 第三军医大学学报, 2011, 33(2): 173-176.
- KANG Jian-yi, WANG Jian-min, YU Yong-min, et al. Numerical simulation research of thoracic region finite element model loaded by blast wave[J]. Acta Academiae Medicinae Militaris Tertiae, 2011, 33(2): 173-176. (in Chinese)
- [16] 周章涛,刘建湖,裴红波,等. 水下近距和接触爆炸流固耦合作用机理及加载效应研究[J]. 兵工学报, 2017, 38(增刊1): 136-145.
- ZHOU Zhang-tao, LIU Jian-hu, PEI Hong-bo, et al. Fluid-solid coupling mechanism and loading effect of underwater near contact and contact explosion[J]. Acta Armamentarii, 2017, 38(S1): 136-145. (in Chinese)
- [17] Elsayed N M, Attins J L. 爆炸与冲击相关损失[M]. 蔡继峰,译. 北京: 人民卫生出版社 2011.
- Elsayed N M, Attins J L. Explosion and impact related losses[M]. CAI Ji-feng, translated. Beijing: People's Medical Publishing House 2011. (in Chinese)
- [18] 唐献述,王树民,龙源,等. 爆炸空气冲击波对动物伤害效应试验研究[J]. 工程爆破, 2012, 18(2): 104-106, 96.
- TANG Xian-shu, WANG Shu-min, LONG Yuan, et al. Experimental study on the effect of explosion air shockwave on the animal injury[J]. Engineering Blasting, 2012, 18(2): 104-106, 96. (in Chinese)





中北大学  
NORTH UNIVERSITY OF CHINA

科研管理系统

欢迎您:【王海宾】新消息(21) | 退出

首页 我的科研

当前位置 - 我的科研 - 我的项目 - 已立项项目

返回

立项信息 项目成员 到账经费 支出经费 年度经费 变更结题情况 经费预算 经费执行情况

【项目基本信息】

校内编号 *	1910400002MZ
项目编号	201803D221026-4
项目名称 *	基于肠道菌群多样性原理研发替代抗生素的饲料添加剂及其产业化示范
项目性质	纵向

【项目详细信息】

项目来源 *	山西省科技厅	项目类别 *	省重点研发计划 (农业领域)
项目级别	一般项目	项目等级	-请选择-
预期成果形式			
负责人 *	王海宾	学历	博士研究生
职称	副教授	承担部门 *	化学工程与技术学院
手机	18234162468 (如:1599****567)	电子邮件	(如:aa@163.com)
学科门类 *	理工类	二级分类	理科类
学科分类	-请选择-		
项目密级	-请选择-	研究类别	-请选择-
社会经济目标	-请选择-	服务国民经济行业	-请选择-
合同编号			
合同开始日期 *	2018-04-01	合同完成日期 *	2020-12-31
立项日期 *	2019-01-11		
研究期限			
是否合作项目 *	<input checked="" type="radio"/> 是 <input type="radio"/> 否	学校排名	1
合作形式	技术服务		
立项文件文号			
归档状态	未归档	归档日期	

【项目承担单位】

署名顺序	单位名称	省份/国家	地市、区县	联系人	联系人电话、手机
2	大禹生物工程有限公司	山西	运城、芮城县	麻啸涛	18636300040

【项目经费信息】

申请经费(万元)	30.0000	合同总经费(万元) *	10.0000
下拨经费(万元)		财政经费(万元)	
企业自筹经费(万元)		个人自筹经费(万元)	
配套经费(万元)		地方配套经费(万元)	
校内配套(万元)		应到校经费(万元)	
管理费(万元)		项目可用经费总额(万元)	
经费帐号	1910400002MZ		

【上传附件】

申请书附件 提交4





[首页](#) [我的科研](#)

当前位置 - 我的科研 - 我的项目 - 已立项项目

[返回](#)

[立项信息](#)   [项目成员](#)   [到账经费](#)   [支出经费](#)   [年度经费](#)   [变更结题情况](#)   [经费预算](#)   [经费执行情况](#)

【项目基本信息】

项目名称	基于肠道菌群多样性原理研发替代抗生素的饲料添加剂及其产业化示范				
负责人	王海宾	所在单位	化学工程与技术学院		
合同经费	10.0000	(万元)	总到账经费	10.0000	(万元)

【已到账经费记录】单位: (元)

费用项目	到账时间	到账金额	经费卡号	拨款单位	经办人	凭单号
学校管理费	2019-01-11	100000.0		山西省科技厅		

# 山西省重点研发计划项目

## 计划任务书

项目类别: ■ 农业方面

项目编号: 201803D221026-4

项目名称: 基于肠道菌群多样性原理研发替代抗生素的饲料添加剂及其产业化示范

项目负责人: 王海兵

承担单位: 山西大学

项目起止时间: 2018年04月 至2020年12月

填报日期: 2018 年 12 月 21 日

山西省科学技术厅



二零一六年制



项目承担单位	项目名称	基于肠道菌群多样性原理研发替代抗生素的饲料添加剂及其产业化示范				
	通信地址	山西省 太原市 尖草坪区学院路3号				
	法人代表	沈兴全	电话	0351-3922018	传真	0351-3924838
	项目联系人	曹杨	电话	0351- 3921762	E-mail	kyydfqyc@nuc.edu.cn
	职工总数	2339人	中高级以上职称人员数		1969人	
	开户银行	太原市工行迎新街支行		行号	102161000241	
	开户名称	中北大学		帐号(基本)	0502121909024910171	
	单位性质	全额事业单位				
上年末财务状况	总收入 <u>115381.2</u> 万元, 技术性收入 <u>26696.2</u> 万元, 上缴税金 <u>3300</u> 万元, 净利润 <u>43788.7</u> 万元; 总资产 <u>421816.68</u> 万元, 流动资产 <u>105605.25</u> 万元, 固定资产 <u>276816.78</u> 万元, 其中科研装备 <u>13116.5</u> 万元; 资产负债率 <u>11.17%</u> 。					
合作单位	单位名称		联系人	电话	是否有合作协议	
	1. 山西大禹生物工程股份有限公司		麻啸涛	0359-3025000	是	1. 是2. 否
	2.					1. 是2. 否
	3.					1. 是2. 否
项目起止时间		2018年04月 至2020年12月				

项目主要研究人员							
1. 项目负责人							
姓 名	王海宾		性 别	男	出生年月	1975年 12月	
技术职称	副教授		职 务	微生物学 会常务理事	毕业校名	中北大学	
毕业年份	2015		最后学历	博士研究生	专 业	军事化学 与烟火技术	
通讯地址	山西省 太原市 尖草坪区学院路3号中北大学化学工程 与技术学院				邮 编	030000	
联系电话	0351-3921714				手 机	182341624 68	
E-mail	whaibin@nuc.edu.cn				身份证号	142131197 51230701X	
2. 主要研究人员							
姓名	性 别	出生 年月	学位	职称	专业	承担任务	单位
王芳	女	1976年10月	博士	副教授	生物工程	益生菌扩 培与棕榈 粕发酵工 艺研究	中北大学
贾万利	男	1972年07月	硕士	讲师（高校 ）	生物化学 与分子生 物学	生化指标 分析	中北大学
史楠	女	1980年01月	博士	讲师（高校 ）	生物工程	免疫指标 测定	中北大学
王蓉珍	女	1968年07月	学士	教授级高级 工程师	生物化学	动物饲料 营养检测 与分析	中北大学
赵英虎	男	1980年05月	博士	讲师（高校 ）	动物营养 与饲料科 学	动物生长 指标检测	中北大学



项目的经费预算 单位：万元（保留两位小数）

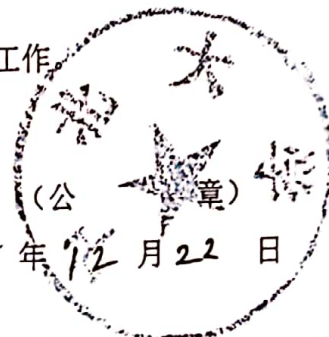
经费来源预算		经费支出预算		
项目	金额	项目	金额	其中：财政专项经费
项目投资合计	10.00	项目支出合计	10.00	10.00
一、省科技厅拨款	10.00	(一) 直接费用	9.10	9.10
2018年度拨款	10	1、设备费	0	0
2019年度拨款	0	2、资料费	0	0
二、其他部门拨款	0	3、材料费	2.5	2.5
其中：国家拨款	0	4、测试化验加工费	0.6	0.6
三、自有资金	0	5、数据或样本采集费	0.2	0.2
其中：企业资金	0	6、燃料动力费	0	0
四、贷款	0	7、差旅使用费	0	0
五、其它资金	0	8、差旅费	1	1
		9、会议、会务费	0.6	0.6
		10、办公费	0	0
		11、国际合作与交流费	0	0
		12、国内协作费	0	0
		13、印刷、出版费	0.5	0.50
		14、知识产权事务费	2.5	2.5
		15、劳务费	1.2	1.2
		16、专家咨询费	0	0
		17、其他支出	0	0
		(二) 间接费用	0.9	0.9
		其中：绩效支出	0.4	0.4

### 项目负责人承诺

- 1、我保证上述填报内容真实、客观，项目组成员切实参与项目的实施；
- 2、我与本项目研究人员将严格遵守国家及山西省科技计划的有关规定；
- 3、积极组织协调项目参与各方认真开展研究工作，完成计划任务书约定的内容；
- 4、积极督促各单位人、财、物等科研保障按时足额到位；
- 5、在项目实施过程中，遵纪守法，并保证接受相关部门的监督检查；
- 6、按要求做好项目过程管理、科技报告编写、结题验收和绩效评价等工作。

项目负责人（签字）

王海宾



2018年12月22日

### 项目承担法人审查与承诺

已按有关规定对计划任务书内容进行了审查，情况属实，并保证做到：

- 1、严格遵守国家及山西省科技计划的有关规定；
- 2、保证在人、财、物和工作时间等方面给予积极支持，特别是自筹经费足额按时到位，按计划任务书约定完成任务；
- 3、协调、督促项目合作单位对项目实施所需的人、财、物和工作时间等条件给予支持；
- 4、督促项目组按期完成项目的结题验收工作。

法定代表人（签字）



2018年12月22日

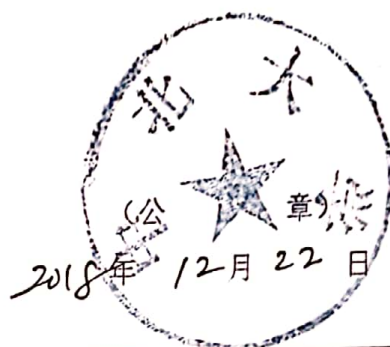
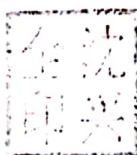
任务书签订意见

项目承担单位:

项目负责人(签字)

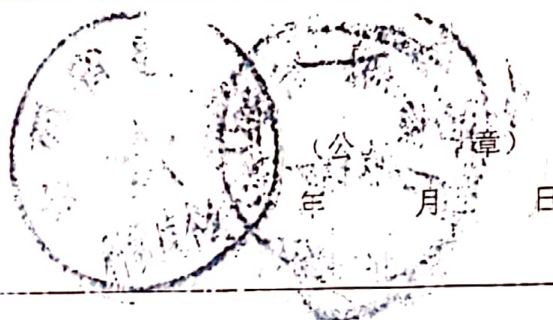
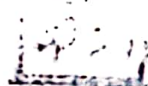
王海兵

单位负责人(签字)



项目组织单位:

负责人(签字)



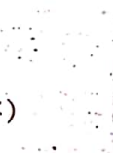
项目管理机构:

同意

项目专管员(签字)



负责人(签字)



科技厅审定意见

项目主管处室负责人(签章) (科技计划专用章)



2018年12月24日



[返回](#)

立项信息    项目成员    到账经费    支出经费    年度经费    变更结题情况    经费预算    经费执行情况

## 【项目基本信息】

校内编号 \* 2110400019HX

项目名称 \* 集成式全身污染监测仪结构设计

项目性质 横向

是否环评

☐ 是 ☒ 否

## 【项目详细信息】

项目来源 \* 计划外

项目类别 \*

技术开发

预期成果形式 样机

负责人 \* 王海宾

学历

博士研究生

职称 副教授

承担部门 \*

化学工程与技术学院

手机 18234162468

(如:1599\*\*\*\*567)

电子邮件

whaibin@nuc.edu.cn (如:aa@163.com)

学科门类 \* 理工类

二级分类

工科类

学科分类 化学工程

项目密级 非密

研究类别

开发研究

社会经济目标 环境保护

服务国民经济行业

-请选择-

合同编号

合同开始日期 \* 2021-06-04

合同完成日期 \*

2021-06-30

立项日期 \* 2021-06-07

委托单位 \* 山西中辐核仪器有限责

委托联系人

委托联系方式

(如:1599\*\*\*\*567)

委托联系地址

山西省太原市尖草坪区

国别 \* 国内

省份 \*

山西

地市 -请选择-

区县

-请选择-

研究期限 4个月

是否合作项目 \* ☐ 是 ☒ 否

立项文件文号

归档状态 未归档

归档日期

## 【项目经费信息】

合同总经费(万元) \* 23.0000

合同签订日期

2021-03-15

下拨经费(万元) 0

配套经费(万元)

管理费(万元)

项目可用经费总额(万元)

经费帐号 2110400019HX

## 【上传附件】

合同书附件 技术开发合同

结题证书 暂无

正式合同附件 暂无

正式结题证书 暂无

备注  
(限120字)



当前位置 - 我的科研 - 我的项目 - 已立项项目

[返回](#)

立项信息    项目成员    到账经费    支出经费    年度经费    变更结题情况    经费预算    经费执行情况

【项目基本信息】

项目名称	集成式全身污染监测仪结构设计				
负责人	王海宾	所在单位	化学工程与技术学院		
合同经费	23.0000	(万元)	总到账经费	18.4000	(万元)

【已到账经费记录】单位：(元)

费用项目	到账时间	到账金额	经费卡号	拨款单位	经办人	凭单号
学校管理费	2021-06-07	92000.0		山西中辐核仪器有限责任公司		
学校管理费	2021-09-07	92000.0		山西中辐核仪器有限责任公司		

合同编号：

## 技术开发合同

项目名称： 集成式全身污染监测仪结构设计

委托方（甲方）： 山西中辐核仪器有限责任公司

受托方（乙方）： 中北大学

签订时间： 2021-3-15

签订地点： 太原

有效期限： 2021-6-30

中华人民共和国科学技术部印制

# 技术开发合同

委托方(甲方): 山西中辐核仪器有限责任公司

住所地: 山西太原高新技术开发区长治路 420 号

法定代表人: \_\_\_\_\_

项目负责人: 张佳

联系方式：13834552977

通讯地址: 山西太原高新技术开发区长治路 420 号

电话: 0351-2203549 传真: 0351-2203549

电子信箱: \_\_\_\_\_

受托方（乙方）： 中北大学

住所地: 山西省太原市学院路3号中北大学

法定代表人: \_\_\_\_\_

项目负责人: 王海宾

联系方式：18234162468

通讯地址: 山西省太原市尖草坪区学院路3号

电话: \_\_\_\_\_ 传真: \_\_\_\_\_

电子信箱: whaibin@nuc.edu.cn

本合同甲方委托乙方研究开发集成式全身污染监测仪结构设计项目，并支付研究开发经费和报酬，乙方接受委托并进行此项研究开发工作。双方经过平等协商，在真实、充分地表达各自意愿的基础上，根据《中华人民共和国合同法》的规定，达成如下协议，并由双方共同恪守。

**第一条** 本合同研究开发项目须达到以下技术指标:

材料；

3. 其他协作事项：乙方应及时向甲方汇报研发进度。

本合同履行完毕后，上述技术资料按以下方式处理：甲方拥有。

**第五条** 甲方应按以下方式支付研究开发经费和报酬：

1. 研究开发经费和报酬总额为 ¥230000 元（含税），即人民币贰拾叁万元整（含税）。

其中：

(1)设计费 30000 元

(2)减振器购置费 20000 元

(3)不锈钢钣金加工费 135000 元

(4)不锈钢非标件机械加工费 35000 元

(5)“六性”分析报告撰写 10000 元

2. 研究开发经费由甲方 分期（一次、分期或提成）支付乙方。具体支付方式和时间如下：

(1) 签订合同后支付 40%；

(2) 设计图纸确定，发出加工前支付 40%；

(3) 项目验收达标后支付其余 20%；

方开户银行名称、地址和帐号为：

中北大学

开户银行：太原市工行迎新街支行

地址：山西省太原市尖草坪区学院路 3 号

帐号：0502 1219 0902 4910 171

**第六条** 本合同的研究开发经费由乙方以 第五条约定方式 的方式使用。甲方有权以 查询 的方式检查乙方进行研究工作



该研究开发成果相关的技术服务。

**第十六条** 双方确定,甲方有权利用乙方按照本合同约定提供的研究开发成果,进行后续改进。由此产生的具有实质性或创造性技术进步特征的新的技术成果及其权属,由双 (甲、乙、双)方享有。

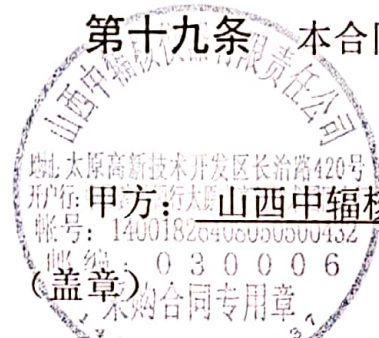
**第十七条:** 双方因履行本合同而发生的争议,应协商、调解解决。协商、调解不成的,确定按以下第2种方式处理:

1. 提交\_\_\_\_\_所在地区\_\_\_\_\_仲裁委员会仲裁;

2. 依法向人民法院起诉。

**第十八条** 本合同一式三份,具有同等法律效力。

**第十九条** 本合同经双方签字盖章后生效。



甲方: 山西中辐核仪器有限责任公司

法定代表人/委托代理人: 王飞 仙竹 和何 (签名)

年 月 日

乙方: 中北大学

(盖章)

法定代表人/委托代理人: \_\_\_\_\_ (签名)

年 月 日